The efficacy of rare-earth doped V_2O_5 photocatalyst for removal of pollutants from industrial waste water

M. H. Kabir[a,b], M. Z. Hossain[a], M. A. Jalil[a], S. Ghosh[c], M.M. Hossain[a], M. A. Ali[a], M. U. Khandaker[d], D. Jana[e], Md. Motinur Rahman[f], M. Khalid Hossain[f], J. Chowdhury[c], M.M. Uddin[a*]

[a]*Department of Physics, Chittagong University of Engineering and Technology (CUET), Chattogram 4349, Bangladesh*

[b]*Department of Materials Science & Engineering, Chittagong University of Engineering and Technology (CUET), Chattogram 4349, Bangladesh*

[c]*Department of Physics, Jadavpur University, 188, Raja S.C. Mallick Road, Kolkata 700032, India*

[d]*Centre for Applied Physics and Radiation Technologies, School of Engineering and Technology, Sunway University, 47500 Bandar Sunway, Selangor, Malaysia*

[e]*Department of Physics, University of Calcutta, 92 A P C Road, Kolkata-700009, West Bengal, India*

[f]*Institute of Electronics, Atomic Energy Research Establishment, Bangladesh Atomic Energy Commission, Dhaka 1349, Bangladesh*

E-mail: mohi@cuet.ac.bd (Md. Mohi Uddin)

Abstract:

The rare-earth (RE) elements [Holmium (Ho) and Ytterbium (Yb)] doped vanadium pentoxide (V_2O_5) with a series of doping concentrations (1 mol.%, 3 mol.%, and 5 mol.%) have been successfully synthesized using environment-friendly facile hydrothermal method. The effect of RE ions on the photocatalytic efficiency of doped V_2O_5 has also been analyzed from both the experimental and first-principle density functional theory (DFT) methods. The stable orthorhombic crystal structure of doped V_2O_5 confirms by the X-ray diffraction with no secondary phase, and high-stressed conditions are generated for the 3 mol.%. The crystallite size, strain, and dislocation density are calculated to perceive the doping effect on the bare V_2O_5. The optical characteristics have been measured using UV-vis spectroscopy. The absorptions are found to be increased with increasing doping concentrations; however, the bandgap remains in the visible range. The photocatalytic properties are examined for the bare compound with varying pH, with

the highest efficiency exhibited for pH 7. Moreover, it is observed that the RE ions significantly impact the catalytic behaviour of V_2O_5. The degradation efficiency is improved by 93% and 95% for the 3 mol.% of Ho and Yb-doped V_2O_5 samples within 2 hours, respectively, and the mechanism behind these extraordinary efficiencies has been explained thoroughly.

Keywords**:** V_2O_5; Hydrothermal; Photocatalysis; Methylene blue; Rare-earth ions; DFT calculations.

1. Introduction

One of the most insistent and concerning issues on the earth is water pollution, which has been rising sharply day by day. The textile, pesticide, tanning, and dye industries are the leading polluters of surface water. Unfortunately, natural fighters, such as bacteria or viruses, cannot heal this chemically tainted wate [1] r. However, one of the effective ways to remedy this problem is photocatalytic materials, which can generate free radicals and decompose these pollutants more easily with the aid of solar radiation at ambient temperature[2,3]. The nanoscale metal oxide and their nanocomposites have been considered the best candidates for photocatalysis due to their extended surface area and recyclability [4]. Some commonly used photocatalysts are TiO_2, ZnO, Fe_2O_3, SnO_2, VO_x, MoO_x, etc [5,6].

The Vanadium pentoxide (V_2O_5), a compound of VO_x family, has been an emerging applicant in recent years in the field of lithium-ion batteries, solar cells, gas sensors, catalysts, and optoelectronics due to its high physicochemical stability, large absorption efficiency in the solar spectrum, and non-toxic nature along with biocompatibility[7–10]. It has an orthorhombic structure with a direct band gap of 2.2-2.8 eV, which makes it suitable for photocatalysis[11,12]. Besides, inherent oxygen vacancies of V_2O_5 lead to the form of many planes of defects arising between the valence band and conduction band, accordingly, creating a quick recombination pathway and aiding the photocatalytic process [13,14]. However, recent findings of V_2O_5 indicate that photo-generated electrons and holes quickly recombine and eventually limit photodegradation efficiency. To achieve a highly efficient photocatalytic reaction, it is utterly necessary to improve

the numerous electron-hole pairs that boost charge separation and impede charge carrier recombination[6,15,16].

Previously, cation doping has been used prominently to reduce or resolve the quick recombination problem. Three categories, including the main group of metals (Na[17], Mg[18], Al[19]), transition metals (Ti[20], Mn[21], Fe[22], Co[23], Ni[24], Cu[25], Zn[26], Zr[27], Mo, and Sn[28,29]), and rare-earths (RE) (Y[30], La[31], Ce[32], Nd[33],Ga[34],and Gd[35]) have been documented for cation doping in the V_2O_5 nanoparticles. Almost all the reports dealt with storage capacity and its associated properties. Very few were looking for the enhanced photocatalytic behavior of doped V_2O_5. As pointed out that the main group metals (like Al^{3+}) act as electron sinks in the doped V_2O_5, resulting in its inability to improve the photocatalytic properties [19]. On the other hand, transitional metal doping enhances the oxidizing capability and the number of active sites by altering surface morphology and their band structures; consequently, not being involved in the improvement of the photocatalytic activity [25,35]

The RE elements doping has become a pronounced technique to enhance photocatalytic activity due to its inherent nature of 4f orbitals. Having a partially filled 4f orbital along with an unfilled 5d orbital, they can easily attack organic dyes and pollutants strongly by forming complex compounds [16,36]. Moreover, the RE metals doping can also be modified the bandgap of the catalyst and shift to the visible range, which plays a vital role in improving the photocatalytic activities of the catalyst [31,33]. In addition, the RE doping increases the number of oxygen vacancies in the semiconductor oxides and hence, enhances the newly formed vacancies that can trap the photo-generated electrons, leading to a lower recombination rate of electron-hole pair[34]. Furthermore, Because RE metals have a smaller work function than metal oxides, they are able to pull electrons from the surface of the metal oxides, which speeds up the photocatalytic activity[16]. On account of these points, it is urgent to study the photocatalytic activity of RE ions doped V_2O_5 since very few reports have been published yet in this regard.

The photocatalytic properties of V_2O_5 can also be tuned by controlling its morphological structure, such as nanorods[35], nanodots[37], nanowires[38], nanoflowers[39], etc. This shape-controlled V_2O_5 can be synthesized by different methods, such as sol-gel synthesis, hydrothermal method,

chemical vapor deposition, electrochemical deposition, pulsed laser ablation, solution combustion, etc.[40–42] Among them, the hydrothermal method is reported to be a highly productive, low-cost, easy-handling, and environment-friendly synthesis procedure. Moreover, its low-temperature operating system aids in guiding the crystallinity and morphology of the compounds that eventually regulate photocatalytic activity [24,38]

Although various metal doping has been implanted into the V_2O_5 for enhancing energy storage performance, a few reports have been focused on their photocatalytic performance. Rigorous studies of the photocatalytic performance of V_2O_5, especially RE elements doping, are required to suggest V_2O_5 as a potential catalyst for pollutants or dye degradation. In this paper, we are introducing RE elements, such as Holmium (Ho) and Ytterbium (Yb) for the first time with different weight ratios (1, 3 & 5 mol.%) into the V_2O_5 nanoparticles by following hydrothermal technique to evaluate their photocatalytic efficiency. Here, we also explore the effect of doping on the structural and morphological properties of pristine V_2O_5 from both the experimental as well as first-principle DFT calculations. Besides, optical properties, such as absorbance, reflectance, and optical bandgap, are studied thoroughly to explain its dye degradation performance.

2. Experimental and Computational Details

2.1 Chemicals

Commercially available ammonium metavanadate (NH_4VO_3), holmium nitrate pentahydrate ($Ho(NO_3)_3 \cdot 5H_2O$) and ytterbium nitrate pentahydrate ($Yb(NO_3)_3 \cdot 5H_2O$) were used without any further purification. All the chemicals are purchased from Sigma Aldrich (Germany) chemicals.

2.2 Synthesis Procedure of RE-doped V_2O_5

The pristine, Ho-doped, and Yb-doped V_2O_5 were synthesized by facile hydrothermal technique. The steps of the whole procedure are illustrated in Figure 1. Ammonium metavanadate was dissolved into an equal ratio of de-ionized (DI) water and ethanol to make a 1M concentration. Ho/Yb precursor was added as a doping element into the solution with 1 mol.%, 3 mol.%, and 5 mol.%. Then, a certain pH level was maintained for making an acidic medium by adding nitrite acid (10wt.%). This solution was stirred for 1 hour at room temperature and transferred to a Teflon-

lined hydrothermal autoclave for 24 hours at 100 °C. After the reactions, the products were washed several times with DI water and ethanol using centrifugation and dried for 6 hours in an oven. Finally, the annealing was done at 500 °C for 2 hours to improve the crystallinity of the final product.

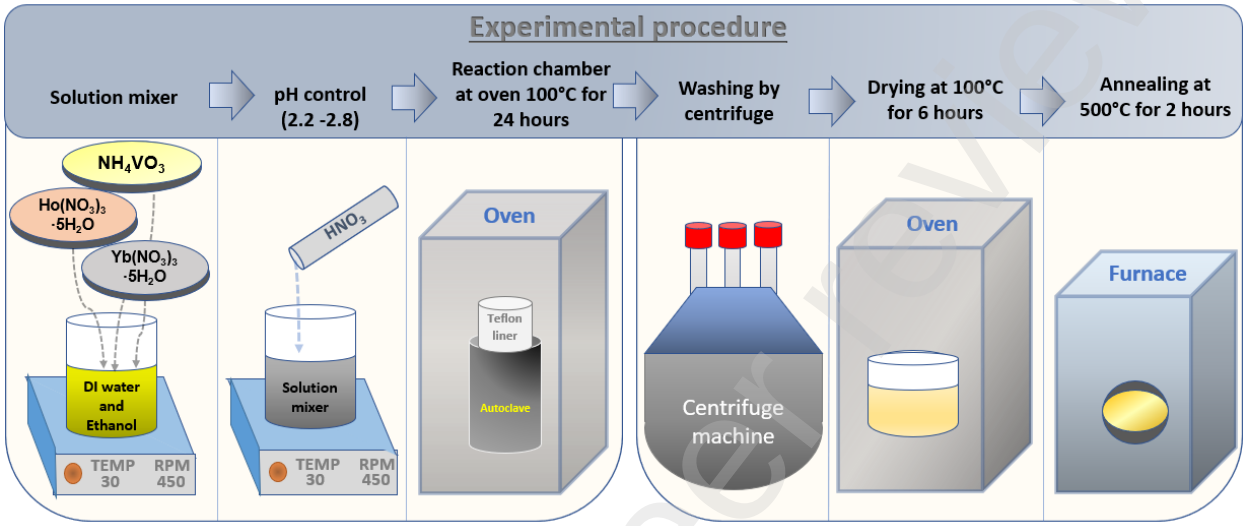

Figure 1: Experimental procedure of preparing pure and Ho/Yb doped V_2O_5

2.3 Characterization Techniques

The X-ray diffraction (XRD) technique was used for structural analysis through the Rigaku Smart Lab diffractometer with Cu-Kα radiation (λ=1.5406 Å). Surface morphology was studied by SEM images TESCAN VEGA 3. Qualitative chemical analysis was acquired by Energy dispersive spectroscopy. The UV-Vis absorption spectra were measured in a Lambda 650 Perkin Elmer spectrophotometer in the wavelength range from 200 to 900 nm.

2.4 Photocatalytic Performance Test

The photocatalytic performance of pure and Ho/Yb doped V_2O_5 was evaluated by adding methylene blue (MB) as a sample of industrial pollutants. A 300 W Xenon lamp was used as the visible light source, and a solar simulator was attached to filter out UV light ($\lambda > 420$). We maintained a distance of 20 cm between the light and to sample. The instrumental setup for evaluating photocatalytic activity is illustrated in Figure 2. For each experiment, 10^{-4} M

concentration of MB solution was prepared into 200 ml DI water. A 200 ppm catalyst concentration was added to investigate the effects of pH variation. On the other hand, 500 ppm concentration was used to observe the improvement of photodegradation efficiency in the presence of RE doping in the V_2O_5 particles.

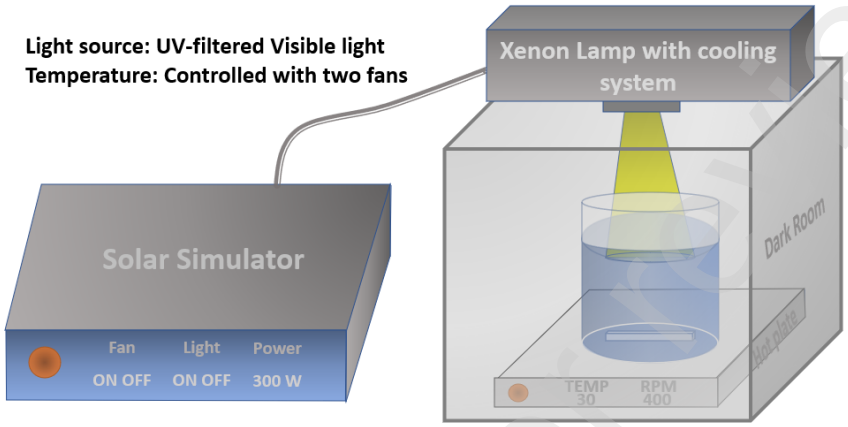

Figure 2: Equipment arrangement for the photocatalytic performance measurement

After adding the catalyst, the solution was stirred for 30 min in the dark condition to develop an adsorption-desorption equilibrium between the V_2O_5 and MB. After turning the light ON, absorption spectra were measured at 20-minute intervals. For this, a 10 ml solution was separated from the original solution and then centrifuged the liquid at 5000 rpm for 5 mins.

2.5 Computational methodology

The first-principle calculations have been accomplished within the DFT framework with the aid of the Quantum ESPRESSO software [43,44]. The crystal structure for the primitive orthorhombic *Pmmn* phase of V_2O_5 (VO) compound, as attained from experimentally determined X-ray powder diffraction data under ambient pressure (P = 0 GPa) [45], has been initially optimized using the variable-cell relaxation method as implemented under Broyden-Fletcher-Goldfarb-Shanno scheme [46–49]. The projector augmented wave (PAW) pseudopotentials [50] has been taken into account to consider the electron-ion interactions and the exchange correlation (XC) terms of the pseudopotentials have been incorporated using the generalized gradient approximation (GGA) followed by Perdew-Burke-Ernzerhof for solids (PBEsol) functional [51]. To calculate the defect

formation energies (ΔE_{df}) of Ho and Yb-doped VO compounds, a 2 × 2 × 2 supercell geometry of pristine VO system has been considered. The Ho/ Yb atoms are systematically doped by replacing V atoms of the said optimized supercell to attain the 3% ($Ho_{0.06}V_{1.94}O_5$, $Yb_{0.06}V_{1.94}O_5$) and 5% ($Ho_{0.1}V_{1.9}O_5$, $Yb_{0.1}V_{1.9}O_5$) Ho/ Yb-doped VO compounds. The valance electrons $3d^3 4s^2$, $2s^2 2p^4$, $4f^{10} 5d^1 6s^2$ and $4f^{13} 5d^1 6s^2$ for V, O, Ho and Yb atoms respectively of the systems are considered as plane waves with kinetic energy cut-off of 60 Ry. The crystal structures of pristine, Ho and Yb-doped VO compounds are allowed to relax until the convergence criteria of Hellmann–Feynman force and total electronic energy reach to 10^{-3} Ry/Bohr and 10^{-8} Ry respectively at P = 0 GPa. While a gamma-centered **k** – point mesh of 10 × 10 × 10 Monkhorst-Pack grid has been framed for geometry optimization and self-consistent-field calculations, a denser mesh of 20 × 20 × 20 grid has been considered for electronic band structures (E-**k** diagram) and projected atomic density of states (PDOS) calculations of the said compounds. To precisely estimate the electronic band gap (E_g) of the systems the on-site Coulomb interaction term +U = 4.0 eV for 3d electron of V atom have been considered throughout the calculations [52].

3. Result and Discussions

3.1 Structural Properties

Figure 3(a) presents the XRD patterns of Ho-doped and Yb-doped V_2O_5, along with the pristine condition of V_2O_5. It is observed that all peaks of the XRD patterns are matched with standard XRD patterns of JCPDS #41-1426, claiming a stable orthorhombic structure has been formed[53]. No additional peaks are detected in the XRD patterns, meaning no secondary phases have been identified in the doping samples.

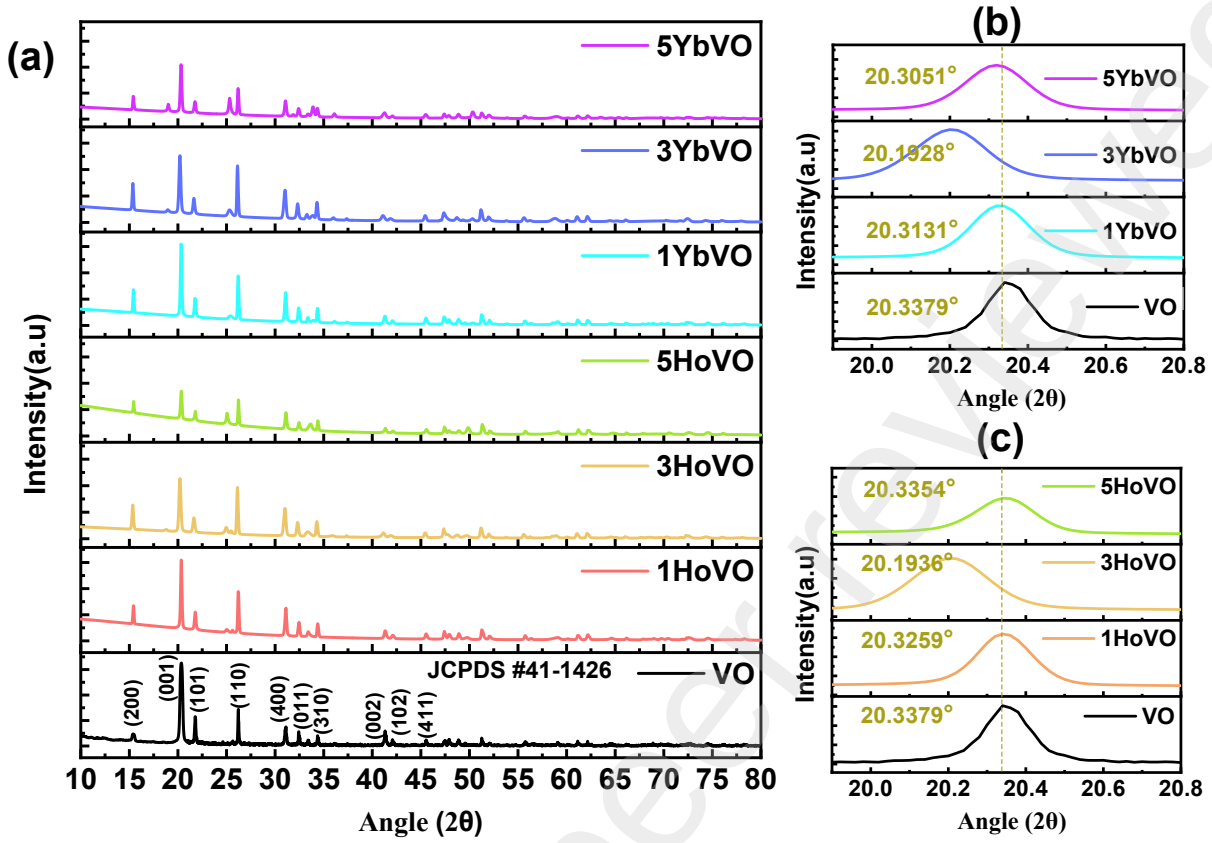

Figure 3: (a) XRD patterns(a) in the range of 10 -80 degrees, (b-c) magnified pattern in the range of 20-20.8 degrees of all the doped and undoped V_2O_5 samples

However, the intensity of the peaks of HoVO (Holmium doped V_2O_5) and YbVO (Ytterbium doped V_2O_5) differ from their pure V_2O_5. The intensity of the peaks decreases with increasing doping concentration indicating the lowering of the crystallite size at the expense of the crystallinity of the samples[35]. The difference in the ionic radius between V^{5+} (5.4 nm) and Ho^{3+} (8.9 nm) or Yb^{3+} (8.6 nm) is relatively high, which forms these discrepancies in the crystal structure. It is also observed that the peaks are shifted to lower 2θ values indicating volume expansion occurred in the doped sample compared to pure V_2O_5, in Figure 3(b-c). 3HoVO and 3YbVO depict the highest peak shifts with respect to all the samples and prosecute the largest stored internal energy in these two samples, attributed to the influence of RE-doped ions on the V-O bonds, creating a local mismatch in the V_2O_5 lattice structure.

Table 1: Crystalline parameters of pure and rare-earth doped (Ho/Yb) doped V_2O_5

	Crystallite size (nm)		d- Spacing (Å)		Micro-Strain x 10^{-3}		Dislocation density x 10^{-3} (nm^{-2})	
Doping %	**HoVO**	**YbVO**	**HoVO**	**YbVO**	**HoVO**	**YbVO**	**HoVO**	**YbVO**
0	71.10	71.10	4.363	4.363	2.76	2.76	1.98	1.98
1	52.60	48.90	4.366	4.368	3.73	4.02	3.61	4.19
3	36.40	38.30	4.394	4.394	5.43	5.16	7.56	6.81
5	48.30	45.40	4.364	4.370	4.06	4.33	4.28	4.85

The average crystallite size (D) of the compounds was calculated by the Debye-Scherrer formula, given below -

$$D = \frac{0.9\,\lambda}{\beta\,cos\theta} \qquad (1)$$

Where β is the full-width at half maximum of (001) peak, θ corresponds to the diffraction angle, and λ is the X-rays wavelength of Cu Kα (1.5406 Å). Similarly, the d-spacing (d), micro-strain(ε), and dislocation density (δ) were also calculated using the following equations and presented in Table (1).

$$d = \frac{n\,\lambda}{2\,sin\theta} \qquad (2)$$

$$\varepsilon = \frac{\beta}{4\,tan\theta} \qquad (3)$$

$$\delta = \frac{1}{D^2} \qquad (4)$$

The crystallite size of VO is found to be 71.1 nm, which decreases rapidly with increasing doping percentage for both elements. The lowest crystallite size value is obtained for 3HoVO and 3YbVO, indicating a decrease in the particle size for 3% doping, which can be explained by the fact that doping ions provide new nucleation sites for particles' formation, which alters the homogeneous nucleation to heterogeneous nucleation. Heterogeneous nucleation is faster than homogeneous nucleation, eventually decreasing the particle size. A similar trend was reported for Cobalt doping in V_2O_5 [54]. It is reported that the interlayer distance of Zr-doped and Ti-doped V_2O_5 nanorods increases due to their large cation size. A similar trend is observed for the present case. The interspacing increases with increasing doping (both Ho and Yb) percentage. The highest spacing estimates for 3mol.% doping concentration of both RE elements in the V_2O_5. Moreover, the micro-strain and dislocation density also followed the trends of d-spacing. Both samples are increased with the increment of the doping elements up to 3 mol.%.

3.2 Morphological Analysis

The surface morphology of the synthesized pure and Ho/Yb-doped V_2O_5 was investigated by taking scanning electron microscopy (SEM) images. Energy dispersive X-ray spectrum (EDX) has also been utilized to confirm the presence of desired elements, such as V, O, Ho, and Yb. In Figure 4a, the particle of V_2O_5 is in irregular shape where agglomeration occurs due to the high surface energy of these particles. The EDX of V_2O_5 is presented in Figure 4b, where no additional peaks are observed except V and O. Besides, the atomic percentage of the elements confirmed the successful formation of V_2O_5.

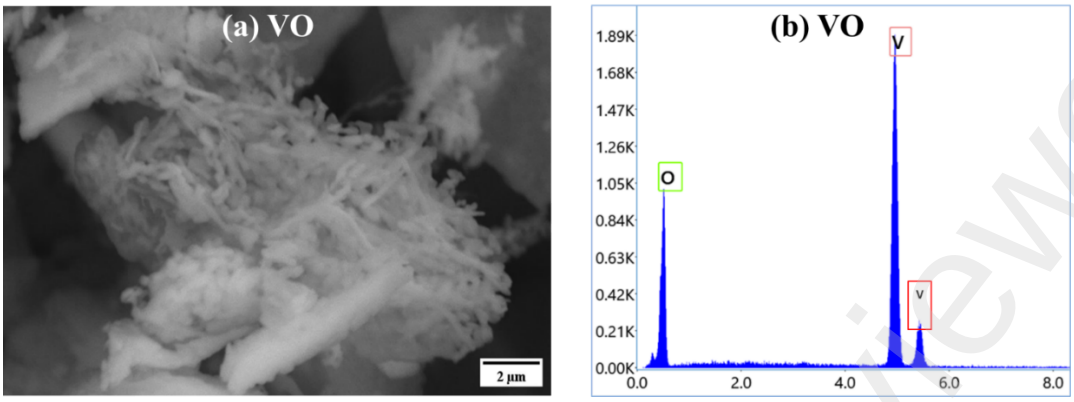

Figure 4: (a) SEM image (b) EDX spectra of pure V_2O_5

The morphology of the particles has been significantly changed with increasing Ho/Yb ions doping, as illustrated in Figure 5. The particle size reduces compared with their pristine V_2O_5 for both cases. The finding is highly persuasive as doping elements create new nucleation and promote heterogeneous nucleation, which eventually reduces the chance of the growth of the particle. However, the agglomeration is continued for the doped samples.

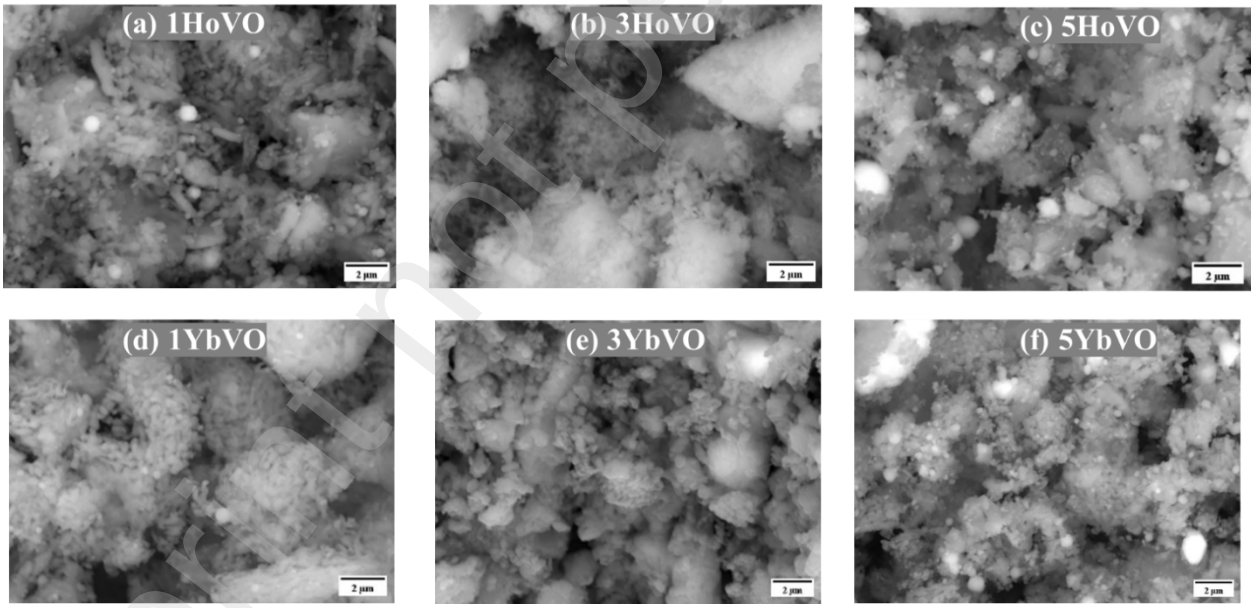

Figure 5: SEM image of (a) 1mol. % Holmium-doped V_2O_5(1HoVO) (b) 3 mol. % Holmium- doped V_2O_5 (3HoVO) (c) 5mol. % Holmium-doped V_2O_5 (5HoVO) (d) 1mol. % Ytterbium -doped V_2O_5 (1YbVO) (e) 3 mol. % Ytterbium -doped V_2O_5 (3YbVO) (f) 5mol. % Ytterbium -doped V_2O_5 (5YbVO).

EDX spectra of Ho/Yb doped V_2O_5 are exhibited in Figure 6. Although the EDX spectra cannot be conclusive in calculating the exact percentage of elements in the overall sample, it can be an excellent way to examine the presence of expected elements. Our expected elements in these spectra have been clearly visible, and the intensity for Ho and Yb increases with increasing the doping percentage.

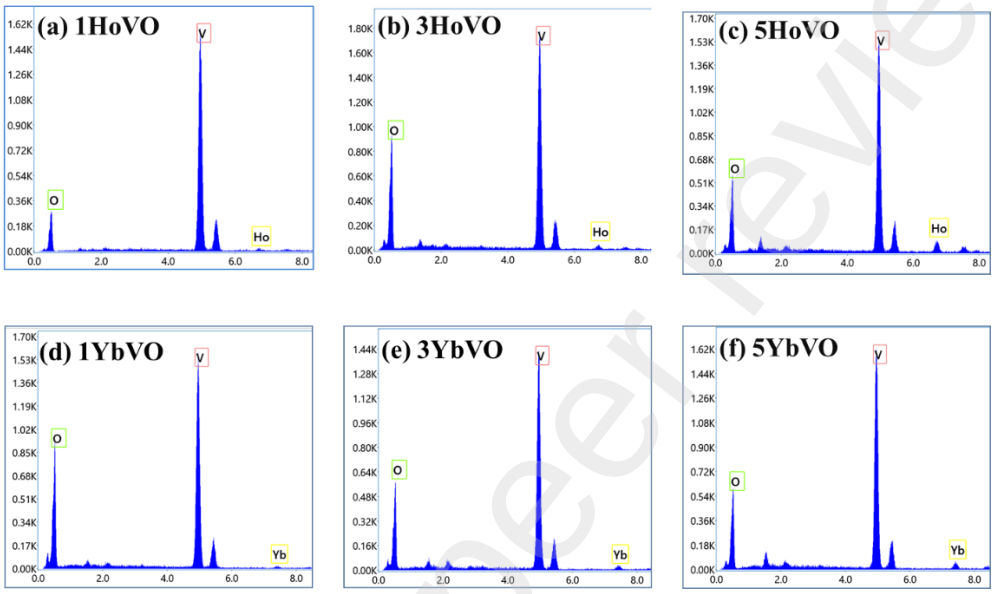

Figure 6: EDX spectra of (a) 1mol. % Holmium-doped V_2O_5(1HoVO) (b) 3 mol. % Holmium- doped V_2O_5 (3HoVO) (c) 5mol. % Holmium-doped V_2O_5 (5HoVO) (d) 1mol. % Ytterbium -doped V_2O_5 (1YbVO) (e) 3 mol. % Ytterbium -doped V_2O_5 (3YbVO) (f) 5mol. % Ytterbium -doped V_2O_5 (5YbVO).

3.3 Optical Characteristics

UV-visible (UV-vis) absorption spectra of pure, Ho-doped, and Yb-doped V_2O_5 are presented in figure 7(a-b). All the samples show strong absorption in the visible range, attributed to the electron transition from O (2p) to V (3d) [35,54]. For the Holmium/Ytterbium doping, the absorption increases in the UV range due to the unfilled orbitals of RE ions. Besides, substituting V^{5+} with Ho^{3+} or Yb^{3+} creates a charge imbalance in the crystal structure, leading to the formation of oxygen vacancies to compensate for the charge imbalance. These defects are also responsible for enhancing the absorption of the doped V_2O_5 samples [53].

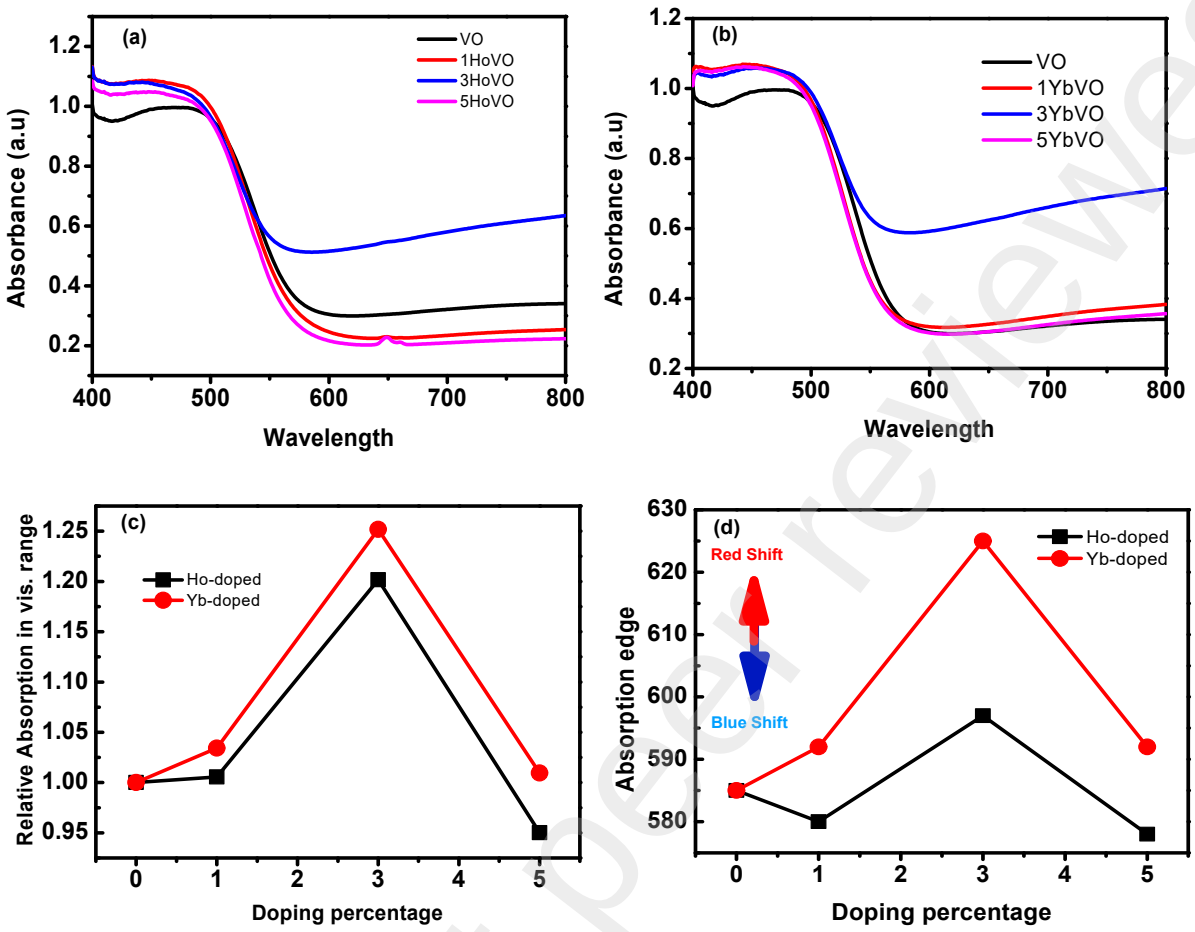

Figure 7: UV-visible absorption spectra for various (a) Ho-doping and (b) Yb Doping. (c) Calculated relative absorption and (d) absorption edge of Ho-doping and Yb Doping

The relative absorption (RA) is an essential parameter to observe the improved solar efficiency of the prepared sample, as shown in figure 7(c) for the doped samples. It is measured by the following equation in the visible range (380 -750 nm):

$$Relative\ absorption = \frac{Average\ absorption\ of\ desired\ sample\ in\ the\ visible\ ran}{Average\ absorption\ of\ pure\ V_2O_5\ sample\ in\ the\ visible\ ra} \quad (5)$$

The RA value increases with the increment of doping percentage for the samples up to 3 mol.% and then drops very sharply to 5 mol.% percentage. The 3YVO shows a higher RA value than 3HVO, indicating higher solar efficiency can be achieved in the visible range. This increment of

the absorption is highly aligned with the strained conditions due to the lattice distortion we discussed in the structural analysis section 3.1. The absorption edge (AE) is another vital parameter to characterize the optical properties of the samples where absorption discontinuity or absorption limit occurs a sharp discontinuity in the absorption spectrum of a substance, and at that point, the energy of an absorbed photon corresponds to an electronic transition or ionization potential. The AE of the samples has been calculated and illustrated in figure 7(d). Increasing the AE value indicates the 'red shift', and decreasing the value means the 'blue shift'. The YVO samples show the 'red shift' for all the doping percentages compared to the parent VO sample, and 3HVO is shown the maximum value of 'red shift'. The finding indicates that Ytterbium-doping expects to be shown better performance than Holmium-doping.

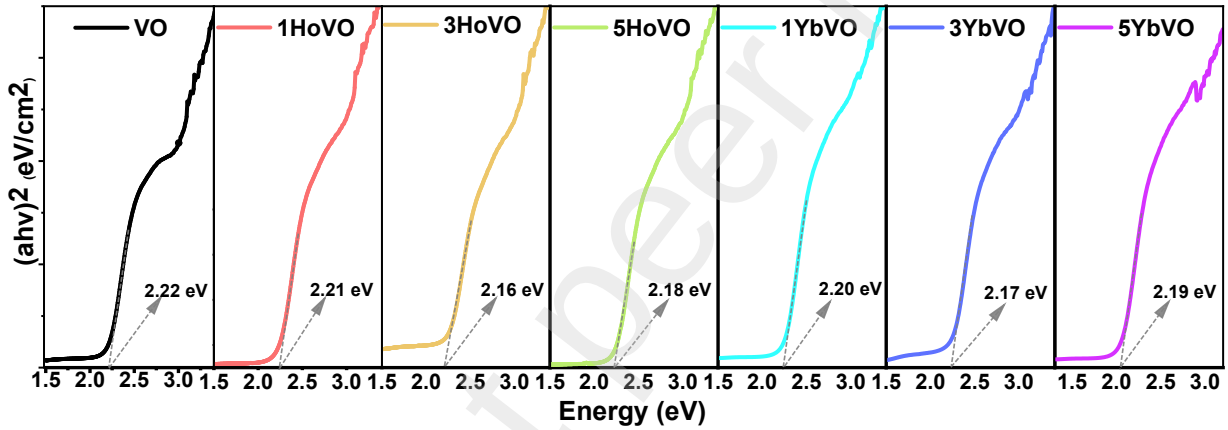

Figure 8: Bandgap measurement of pure, Ho/Yb-doped V_2O_5 sample by using Tauc Formula

The bandgap of the pure and doped samples has been measured using the Tauc relationship,

$$\alpha h\vartheta = A\,(h\vartheta - E_g)^n \qquad (6)$$

Where α is the absorption coefficient, hν defines the photon energy, A suggests a proportional constant, and E_g represents the bandgap of the sample. Two different allowed transitions are classified by using two different 'n' values: n = 2 for direct and n = ½ for indirect bandgap. The calculated bandgap of the samples using the Tauc plot is depicted in figure 8. It is observed that the bandgap reduces for all the doping samples compared to their parent VO. The reduction is caused by introducing defects in the crystal system of pure VO by doping the foreign elements.

These foreign elements form additional energy states within the bandgap that create intermediate paths for electron transitions and delay the electron recombination rate[55]. The maximum decrements of the bandgap are found to be 2.16 eV (3HoVO) and 2.17 eV (3YbVO), which is consistent with our discussion regarding the highest value of RA and AE.

3.4 Photocatalytic Measurements

Methylene blue (MB) is a symbol of pollutants for measuring photocatalysis efficiency. It shows two characteristic peaks in the visible absorption spectra at 613 nm and 664 nm. The peak at 664 nm was considered to evaluate the degradation of the MB. As the decrement of the intensity is proportional to the degradation of the product, the efficiency of photodegradation is calculated by using the following equation:

$$Dye\ removal\ efficiency = \left(1 - \frac{C_t}{C_o}\right) x\ 100 \qquad (7)$$

Here, C_0 represents the initial concentration and C_t defines the concentration of the sampling time. Langmuir Hinshelwood (L-H) kinetics can be used to measure the kinetics of our synthesized catalysts[56], given below:

$$r = -\frac{dC}{dt} = \frac{k_T K C_t}{1 + K C_t} \qquad (8)$$

Where K_r defines the time-dependent reaction rate, K is the equilibrium constant for adsorption. We have used a very low concentration of MB (10^{-4} M), equation (8) can be approximated to the first-order kinetic reaction[57,58], presented in equation (9):

$$ln\left(\frac{C_0}{C_t}\right) = kt \qquad (9)$$

Here, k defines the pseudo-first-order rate constant. This rate constant is calculated from the slope of the $ln\left(\frac{C_0}{C_t}\right)$ vs time curve.

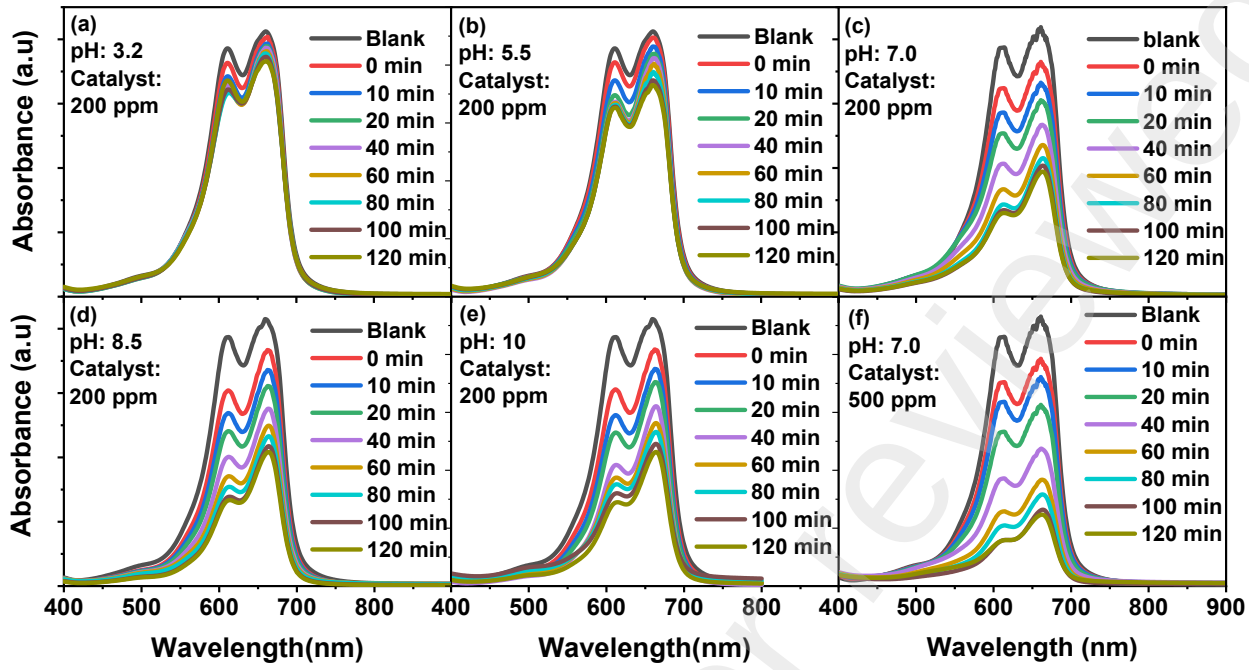

Figure 9: Absorption spectra of MB degradation under various pH levels and catalyst concentrations: (a) as received, (b) pH = 5.5, (c) pH = 7.0, (d) pH = 8.5, (e) pH = 10 and (f) pH = 7 and catalyst = 500 ppm

3.4.1 Effects of pH

Industrial textile dyes contain various contaminants having a wide range of pH levels. So, it is necessary to check the performance of V_2O_5 on the basis of different pH levels. The prepared sample showed a very low pH value (3.3) due to its synthesis process, wherein a pH of 2.5 was maintained. We examine the photodegradation efficiency of V_2O_5 as a function of a wide range of pH levels of 3.3 – 10.0. We set a 200-ppm concentration for the catalyst. The wavelength dependence of absorptions for various pH values is represented in Figure 9.

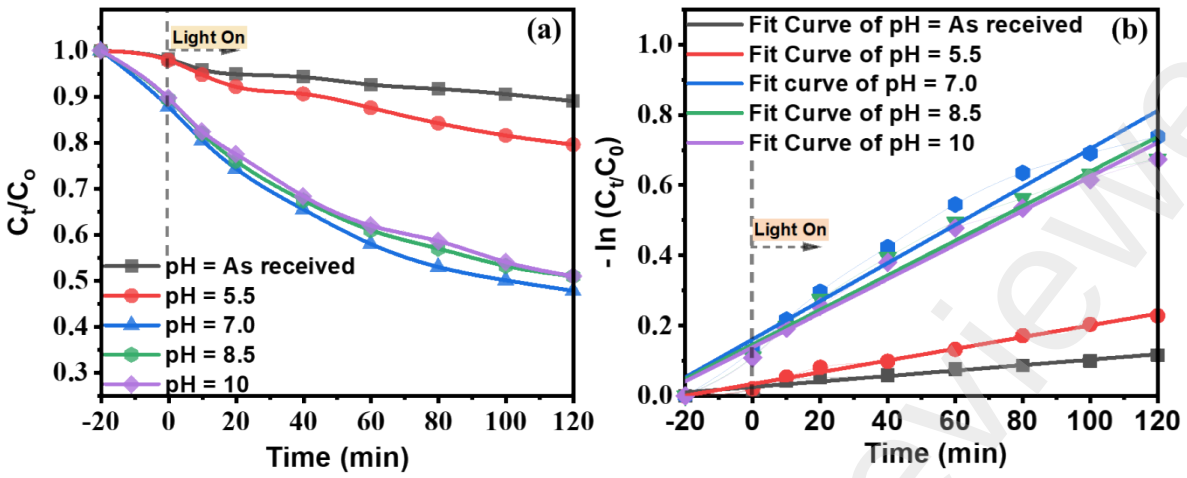

Figure 10: (a) Photocatalytic degradation efficiency and (b) degradation rate constant of MB by V_2O_5 under various pH levels

Time-dependent degradation of the MB in the presence of various pH levels is illustrated in Figure 10(a). The degradation is very low at low pH values (acidic medium), whereas the efficiency improves exponentially from 11% to 52% with a rising pH level from 5.5 to 7.0. The efficiency decreases afterward in the alkaline medium. The Rate constants were calculated for different pH levels, as shown in Figure 10(b). The rate constant curves clearly indicate that the highest degradation is found for pH of 7.0, indicating that the neutral condition or slightly alkaline medium is good for getting better photodegradation efficiency of V_2O_5. The overall degradation efficiency and rate constant values are plotted in Figure 11.

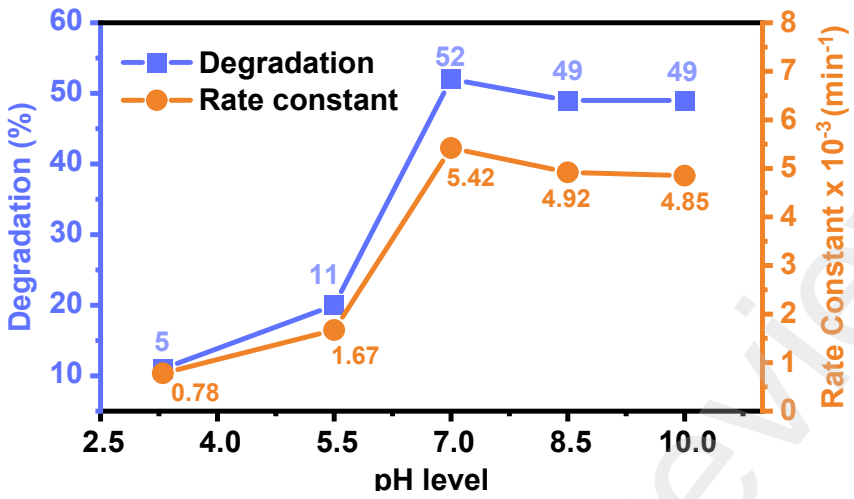

Figure 11: Degradation efficiency (blue) and Rate constants (orange) of V_2O_5 regarding to various pH levels

This phenomenon can be explained by electrostatic interactions between the catalysts and pollutants, as illustrated in figure 12. One of the important parameters to observe the pH effect is the point zero charge (PZC) of the catalysts, where the net charge of the particle surface is zero for a certain pH level [59]. The surface of the particle will be positively charged below this pH level and negatively charged above the pH level. As the MB is cationic, the surface of the catalyst must be negatively charged so that the catalyst can come in contact with the pollutants. At an acidic medium ($pH < pH_{PZC}$), the surface of V_2O_5 is positively charged, repels the MB, and cannot degrade. However, in the neutral or slightly alkaline medium, the surface of catalysts is negatively charged, so adsorption can occur. In our case, the degradation rate was changed dramatically by changing the pH value from 5.5 to 7. So, one can conclude that the PZC of V_2O_5 lies in between pH of 5.5 – 7. It should be noted that the photodegradation efficiency for a very high pH level (11-14) is not considered in this study. However, many reports claimed that the samples show low efficiency at this extreme pH level [24,59,60]. This may be attributed to the neutralization of cationic pollutants due to high OH concentration and restriction to contact with the catalyst.

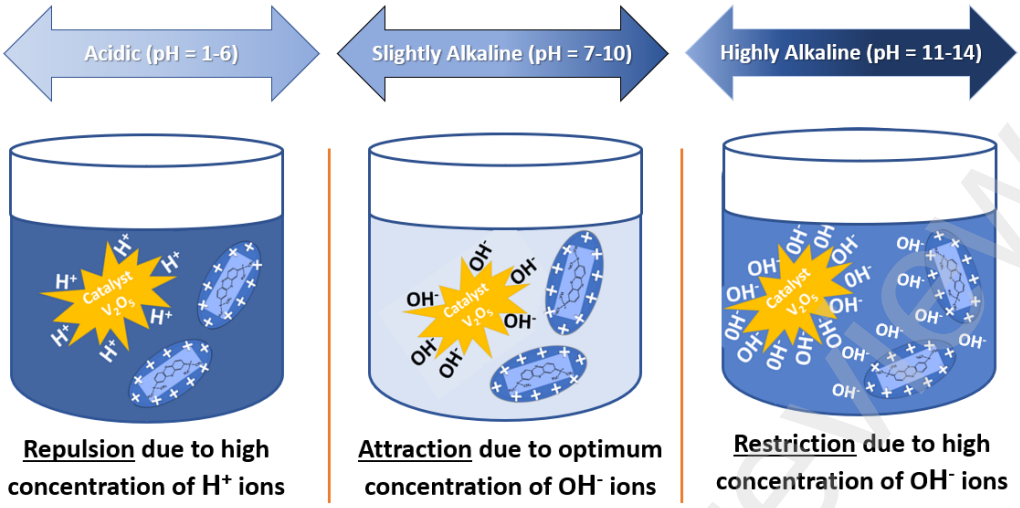

Figure 12: Mechanism of pH effects on photodegradation efficiency of V_2O_5

3.4.2 Effects of Ho-doping and Yb-doping

The photocatalytic degradation efficiency of Ho-doped and Yb-doped V_2O_5 have been measured using the intensity of the characteristic peak of MB in the UV-visible absorption spectra, as presented in Figure 13. A catalyst concentration of 500 ppm is used to observe the efficiency of the samples.

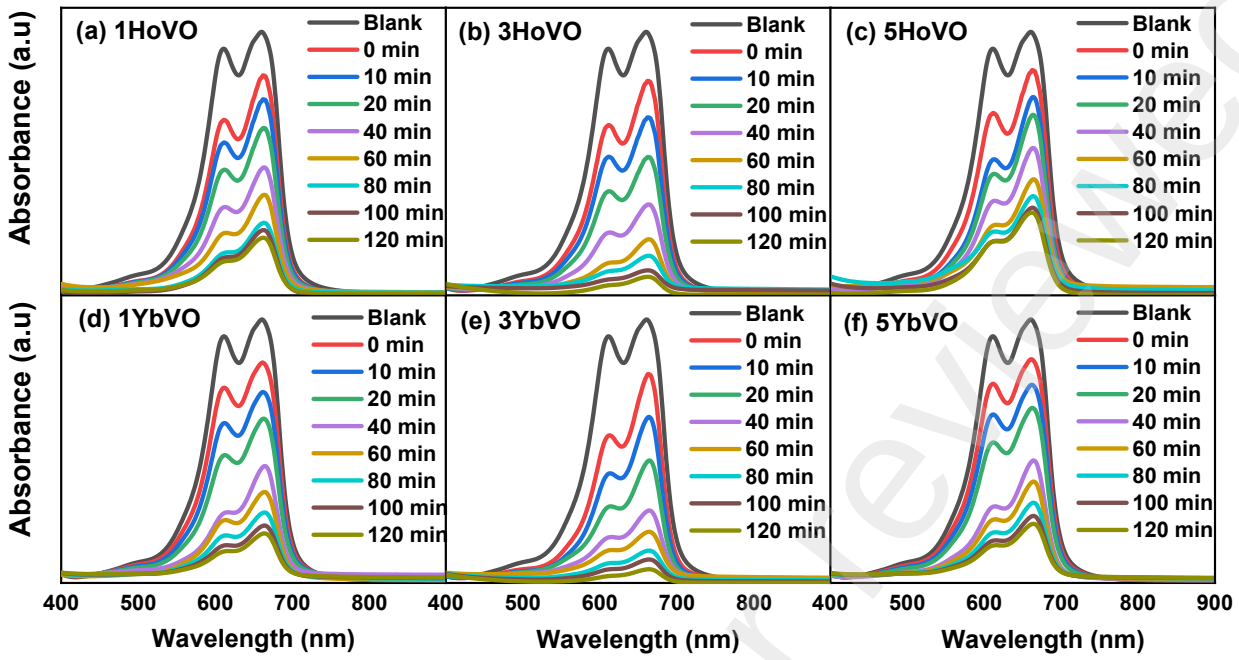

Figure 13: UV-vis absorption spectra of (a) 1mol.% Ho (b) 3mol.% Ho (c) 5 mol.% Ho (d) 1mol.% Yb (e) 3mol.% Yb (c) 5 mol.% Yb-doped V_2O_5

Figure 14(a-b) exhibits the degradation efficiencies and rate constants of 1HVO and 3HVO as a function of time. After 2 hours of visible light irradiation, the degradation increases while it is decreased for 5HVO producing the highest degradation for 3HVO among all samples. The rate constants are found to be 0.012 min^{-1}, 0.020 min^{-1}, and 0.008 min^{-1} for 1HVO, 3HVO, and 5HVO, respectively. Interestingly, the rate constant of 3HVO is almost double compared to its pristine V_2O_5 sample. The degradation percentages are estimated at 78, 93, and 68% for 1HVO, 3HVO, and 5HVO, respectively. Similar trends are observed for Yb doped V_2O_5 crystal structure as depicted in figure 14(c-d). The estimated degradation percentages are 81, 95, and 77% for 1YbVO, 3YbVO, and 5YbVO, respectively. The rate constant is also improved with increasing Yb percentage up to 3 mol.% and then reduced for 5YbVO. Thus, 3HoVO and 3YbVO can be considered promising candidates for photocatalysis.

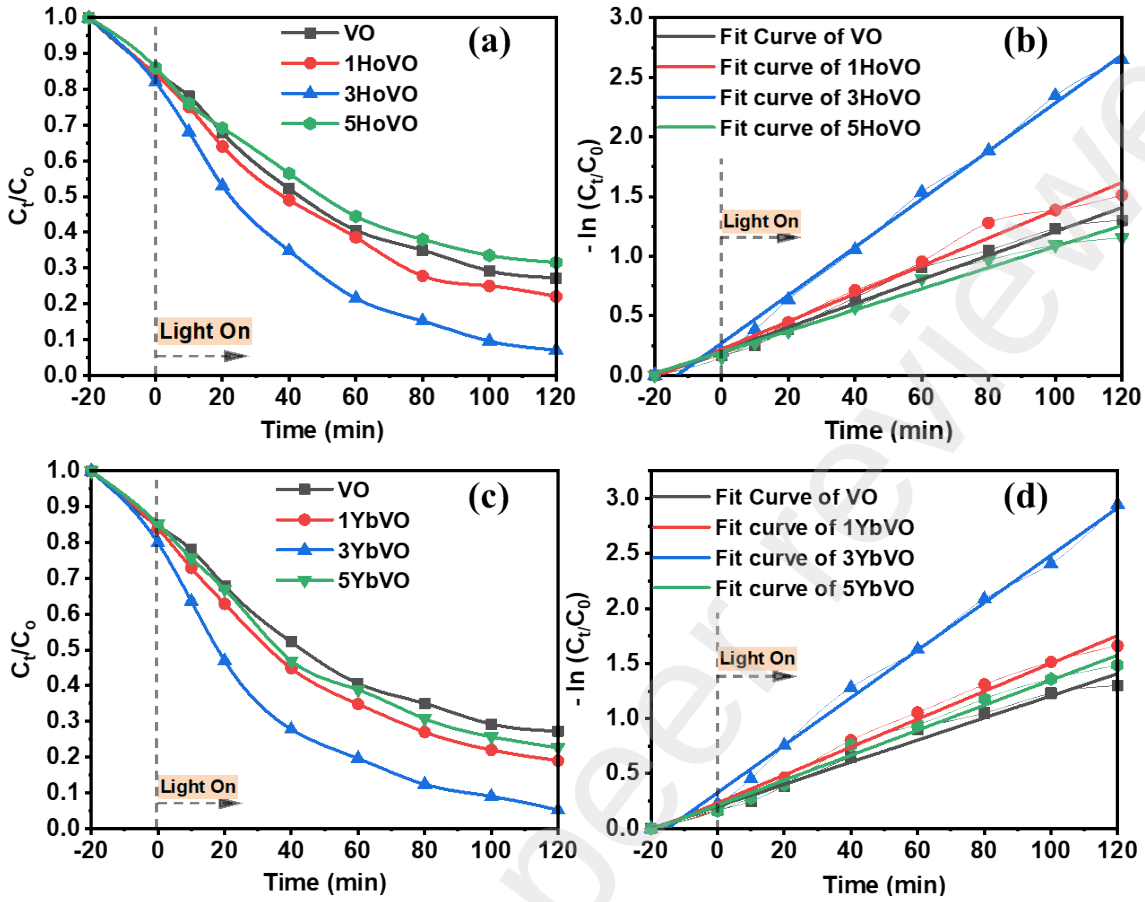

Figure 14: Degradation of MB as a function of time for (a) Ho-doped (c) Yb-doped V_2O_5 samples. Degradation rate constants as a function of time for (a) Ho-doped (c) Yb-doped V_2O_5 samples.

A comparison chart of degradation efficiency and the rate constant is illustrated in figure 15 for better understanding. It is shown that 3 mol.% exhibits the best performance in degrading the pollutants. As the ionic size differences of RE and vanadium are substantial, the crystallinity decreases for high doping percentages such as 5HoVO and 5YbVO. This damaged crystallinity reduces the light absorption in the visible range (Figure 7), consequently reducing the degradation efficiency.

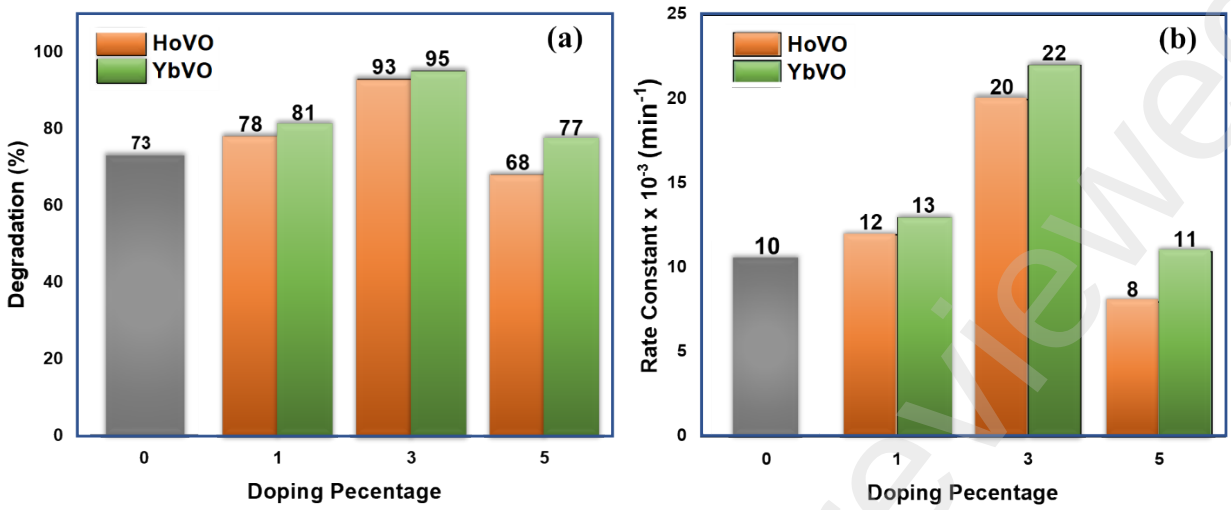

Figure 15: (a) Degradation efficiency (b) degradation rate constant Comparison of pure, Ho and Yb doped V_2O_5.

We have compared our results with available reported RE elements doped V_2O_5, as depicted in Table 2. Various measuring factors affect the degradation efficiency and rate constant such as catalyst concentration, pollutants concentration, degradation time, and energy source. A high concentration of catalyst and a low concentration of pollutants exhibits a high value of degradation percentage.[33] Instead of using higher MB concentration, we obtain the competitive degradation performance among all the V_2O_5 samples. Although Nd^{3+}-doping showed 99% degradation, the concentration of catalyst was double, the concentration of MB was one order lowers, and the light source was in the UV range. However, our obtained degradation rate constants of 3HVO and 3YbVO are the highest compared to all listed V_2O_5 particles. It is evident that 3HoVO and 3YbVO are the best candidates for photodegradation in V_2O_5.

Table 2: An overview of the effects of various ions on V_2O_5 for the photodegradation efficiency of MB

V_2O_5 Catalysts with various doping	Catalysts Conc. (ppm)	MB Conc. (Molarity)	Light Source	Degradation efficiency (%)	Rate constant (min^{-1}) x 10^{-3}	Ref
5 wt.% Gd	100	1.6 x 10^{-5}	Visible light	46	5.50	[35]
5 wt.% Ti	200	1.0 x 10^{-5}	Visible light	82	14.0	[53]
3 mol.% Sn	200	-	Visible light	95	15.3	[28]
5 wt.% Co	500	1.0 x 10^{-4}	Visible light	91	20.0	[54]
7 mol.% Nd	1000	1.6 x 10^{-5}	UV light	99	14.0	[33]
3 mol.% Ho	500	1.0 x 10^{-4}	Visible light	93	20.0	This
3 mol.% Yb	500	1.0 x 10^{-4}	Visible light	95	22.0	This

3.5 Plausible Mechanism of degradation

The possible mechanism of degradation of pollutants using the catalyst and dye MB is illustrated in figure 16. The photons eject electrons from the valence band (VB) of the catalyst surface and move to the conduction band (CV). The recombination occurs between the electron and the hole itself or by the surface charges. Precisely controlling the recombination rate measures the performance of photocatalysis.

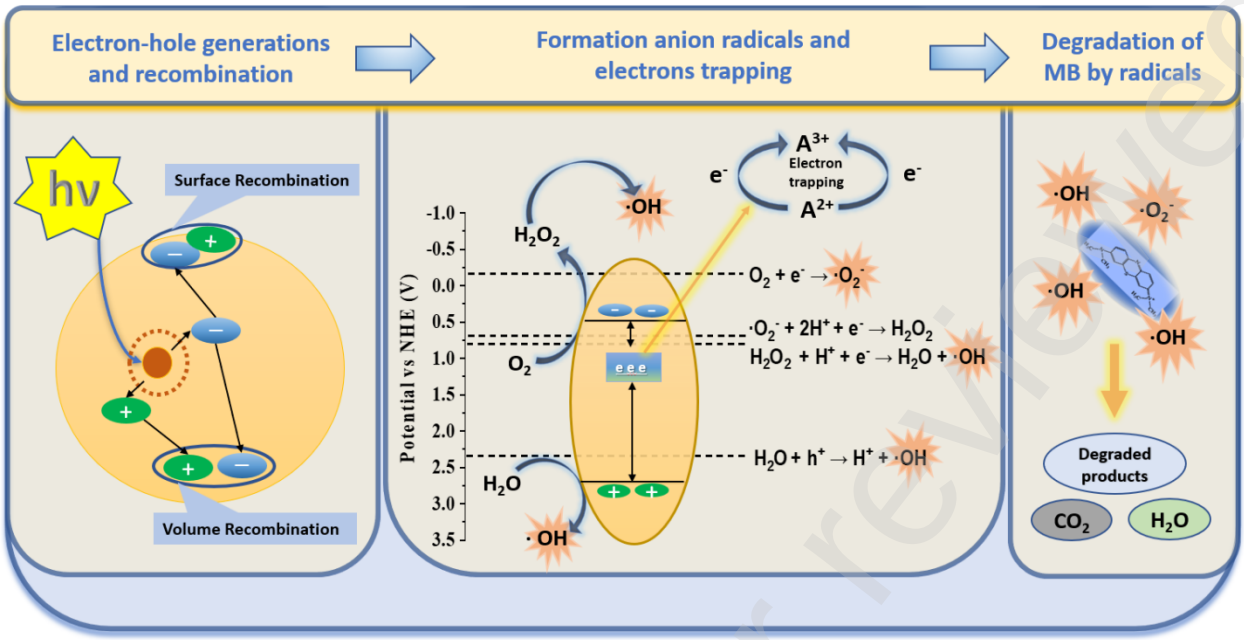

Figure 16: Schematic diagram demonstrating how rare-earth doped V_2O_5 degrade the pollutant efficiently

The potential of the conduction band (E_{CB}) and valance band (E_{VB}) for the V_2O_5 can be calculated by the following equations[60],

$$E_{CB} = \chi + E_C - 0.5\, E_g$$

$$E_{VB} = E_g + E_{CB}$$

Here, χ is the electronegativity of the V_2O_5 (6.1 eV)[61], E_g defines the bandgap of the V_2O_5 (2.22 eV), and E_C represents the energy of free electrons in the hydrogen scale (4.5 eV). The data provides the value of 0.49 and 2.71 eV for E_{CB} and E_{VB}, respectively. Since the addition of doping elements did not change the bandgap in a wide range, the E_{CB} and E_{CB}will remain almost the same as the undoped sample. However, these doping elements create various defects by forming interstitial oxygen and vacancies of vanadium, which introduce additional energy states within the bandgap. These energy states are considered at trapping sites to suppress the electron-hole recombination and lengthen the lifetime of photo-excitons.

Apart from the bandgap reduction and defect formation phenomena, the RE ions form complex compounds with the organic dye that also perpetuate the pollutant's degradation reaction. It is attributed to having partially filled 4f orbital in the electronic configuration of the RE elements. Moreover, the work function of V_2O_5 decreases with increasing RE doping [33]. This decrement suggests that the Fermi level of V_2O_5 moves towards the CB and makes electrons move easier to the acceptors. Finally, these photo-generated electrons can capture oxygen (O_2) and form superoxide radicals ($^{\bullet}O_2^-$), which would continue further reactions to reduce the recombination rate. On the other hand, holes in the valance band can react with water (H_2O) to form hydroxyl radical ($^{\bullet}OH$). These highly reactive radicals attack the pollutants to degrade to generate CO_2 and H_2O. The degradation pathway of MB in the presence of free radicals is thoroughly discussed in the previous report [58]. Thus, the degradation of pollutants has been enhanced in the presence of RE elements.

3.6 Understanding Photocatalytic Activities from First-Principle DFT Calculations

3.6.1 Structural Stabilities of Pristine and Ho, Yb - Doped V_2O_5 Systems

At room temperature (T = 300 K) and under ambient pressure (P = 0 GPa), V_2O_5 crystalizes to primitive orthorhombic phase and belongs to *Pmmn* space group symmetry with space group no. 59. The optimized unitcell geometry of pristine VO, as obtained from the first-principle DFT calculations, is shown in Figure 17(A). The lattice parameters of the crystal system under study have been estimated to be a = 3.575 Å, b = 4.665 Å and c = 11.516 Å which are in close agreement with the experimentally determined X-ray powder diffraction data as reported elsewhere [45].

To introspect the structural stabilities of $Ho_{0.06}V_{1.94}O_5$ (3HoVO), $Yb_{0.06}V_{1.94}O_5$ (3YbVO), $Ho_{0.1}V_{1.9}O_5$ (5HoVO) and $Yb_{0.1}V_{1.9}O_5$ (5YbVO) compounds, the defect formation energies per dopant (ΔE_{df}) have been calculated using the following relation [62,63]:

$$\Delta E_{df} = \frac{1}{N_{Ho/Yb}} [E_{doped} - E_{prisine} - N_{Ho/Yb}(\mu_{Ho/Yb} - \mu_V)] \quad (10)$$

where E_{doped} and $E_{pristine}$ are the total energies of the respective doped and pristine VO compounds, $N_{Ho/Yb}$ represents the number of Ho/ Yb dopants, $\mu_{Ho/Yb}$ and μ_V symbolizes the respective chemical potentials of the isolated Ho/ Yb and V atoms. The optimized supercell geometries of

3HoVO, 3YbVO, 5HoVO and 5YbVO compounds are shown in Figure 17. The ΔE_{df} values for 3HoVO, 3YbVO, 5HoVO and 5YbVO systems are estimated to be -3.74, -3.85, -3.44, -3.50 Ry respectively. From ΔE_{df} values, it is clearly evinced that the doped systems are not only exothermic in nature, but 3HoVO and 3YbVO compounds (3% Ho and Yb – doped VO) are energetically more favourable than 5% Ho/ Yb - doped systems under study. Moreover ΔE_{df} values further suggests that the 3YbVO system is energetically most feasible among the other Ho/ Yb – doped VO compounds.

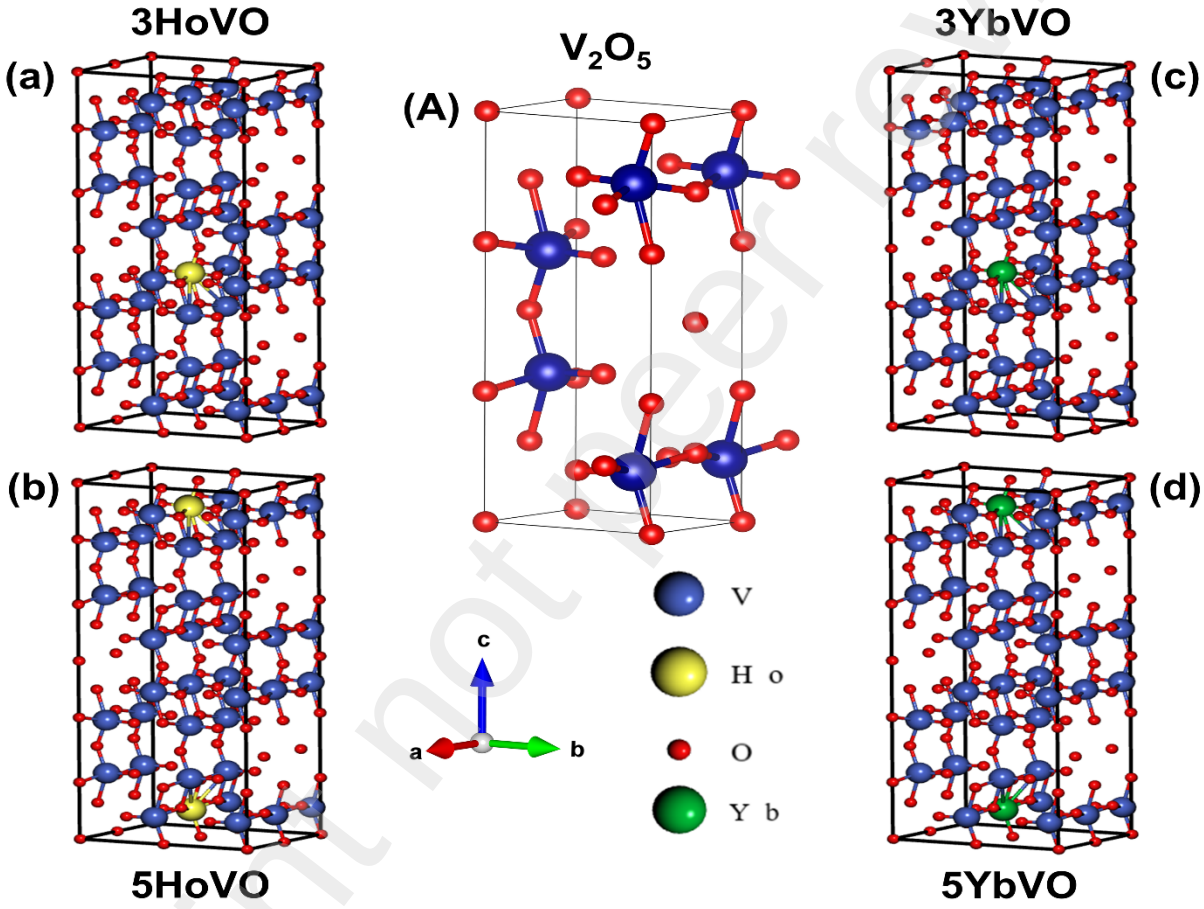

Figure 17. (a) *Optimized unit cell geometry of V_2O_5 compound. Optimized supercell crystal structures of* ***(a)*** *3%,* ***(b)*** *5% Ho – doped V_2O_5 and* ***(c)*** *3%,* ***(d)*** *5% Yb – doped V_2O_5 systems as obtained from the first-principle DFT calculations using GGA-PBEsol level of theory.*

3.6.2 Electronic Properties of Pristine and Ho, Yb - Doped V_2O_5 Compounds

To understand the photocatalytic activities of pristine and Ho, Yb - doped VO systems, the electronic band structures for the pristine and 3% Ho, Yb – doped VO compounds have been estimated. The E-**k** diagrams along Γ→Y→T→Γ→X→U high-symmetry direction for pristine, 3HoVO and 3YbVO systems are shown in Figure 18(a), 18(b) and 18(c) respectively. From Figure 18(a), while top of the valence band of the VO compound is localized at high-symmetry point T, the bottom of the valley depicting the conduction band of the compound are estimated at high-symmetry point Γ in the Brillouin zone. This result implies that the pristine VO system is an indirect band gap semiconductor with E_g ~ 2.22 eV. The estimated value of E_g (~ 2.22 eV), so obtained from PBEsol+U level of theory, is in complete agreement with our experimental observation so obtained from absorption spectrum [*vide supra*, *cf.* Figure 8].

Surprisingly, with 3% Ho and Yb - doping in pristine VO compound, remarkable changes in the E-**k** diagrams have been noticed. The valence band maximum for both 3HoVO and 3YbVO compound are found to be shifted from T to Γ high symmetry points in the Brillouin zone. These results signify that the 3HoVO and 3YbVO systems are direct band gap semiconductors with E_g ~ 2.15 and 2.10 eV respectively. The E_g values of 3HoVO and 3YbVO, so accomplished from the PBEsol+U level of theory, are also in good agreement with our experimental findings where the E_g values of the said compounds are estimated to be ~ 2.16 and 2.17 eV respectively from experimental observations (*vide supra, cf.* Figure 8). The E_g values (~ 2.15 and 2.10 eV) and the direct band gap electronic transitions for 3HoVO and 3YbVO compounds, as obtained from the DFT calculations, fall under the visible region (~ 576.67 and 590.40 nm) of the electromagnetic spectrum. This direct band gap in turn may be responsible behind the enhanced photocatalytic performances of the doped compounds than their pristine counterpart. Interestingly, Figure 18(b) and 18(c) further reveal the presence of flat energy bands in the E-**k** diagrams of 3HoVO and 3YbVO systems. The flat energy bands in general signify larger effective mass and smaller group velocity of the charge carriers, which may suggest an early signature for their potential applications in various research areas such as nonlinear optics, photonics, photolysis and in energy storage devices [64–66].

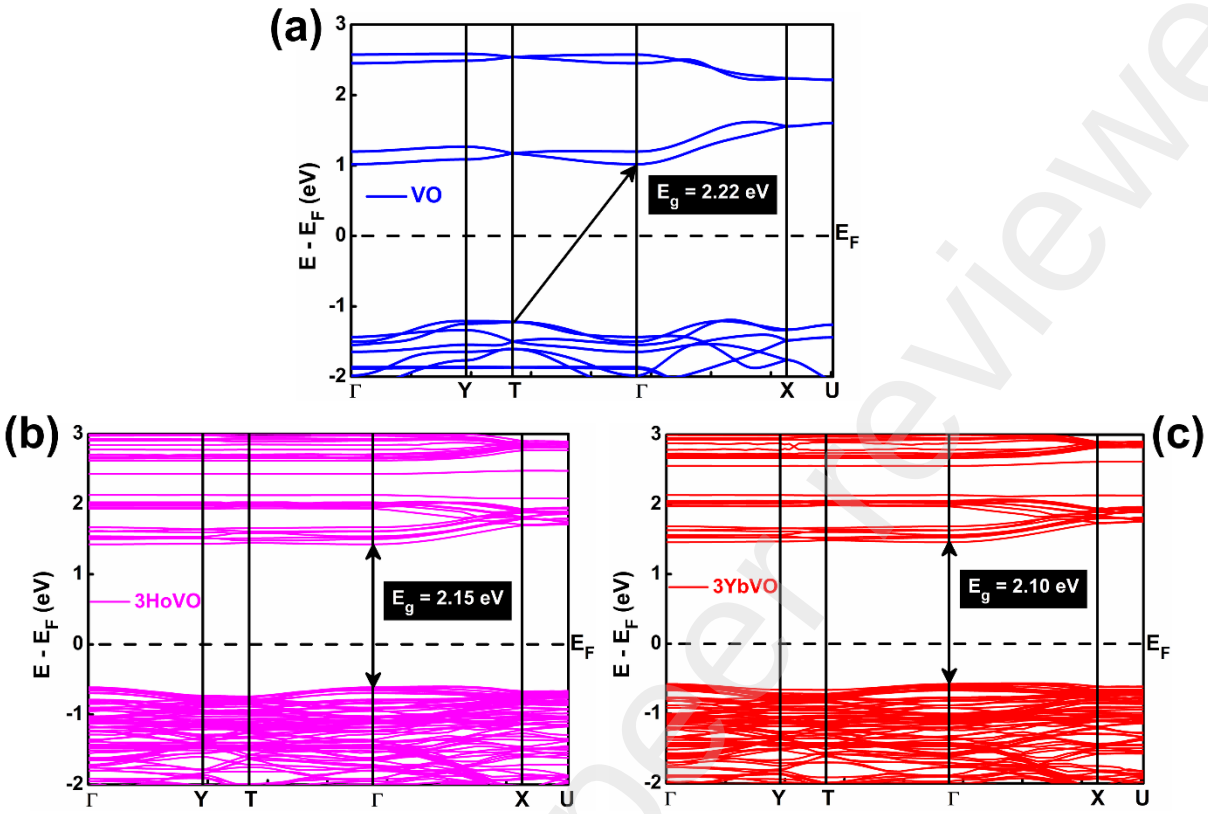

Figure 18. *Electronic band structures along Γ→Y→T→Γ→X→U high-symmetry points of* ***(a)*** *pristine and 3%* ***(b)*** *Ho,* ***(c)*** *Yb - doped V_2O_5 compounds as obtained from PBEsol+U level of theory. [Band gaps are marked with black arrows. E_F represents the Fermi energy level and is designated with horizontal dashed lines.]*

To get deeper insights about the photocatalytic performances of VO, 3HoVO and 3YbVO compounds, the orbital resolved PDOS have been calculated. The results are shown in Figure 19. From Figure 19(a), it is observed that the top of the valance bands, ranging from -2 to 0 eV, are originated mainly from the V-3d and O-2p orbitals, however, relative weight of O-2p orbital is found to be higher than V-3d orbital. This observation primarily suggests strong p-d hybridization between V-3d and O-2p orbitals of the VO system. Moreover, predominant contribution of V-3d orbital has been noticed in the bottom of the conduction bands ranging between 0 and 2 eV. Akin

to E-**k** diagram [*vide supra*, *cf.* Figure 18(a)], depletion of electronic energy states near Fermi energy level (E_F) have been observed in PDOS plot of the VO compound.

Interestingly, upon 3% Ho and Yb - doping in pristine VO compound, remarkable changes in the PDOS plots have also been noticed. The results are shown in the lower panel of Figure 19. From Figure 19(b) and 19(c), definite contributions of Ho-4f, Ho-5d (Yb-4f, Yb-5d) orbitals along with V-3d and O-2p orbitals of 3HoVO (3YbVO) system have been observed near E_F. Relative weights of 4f orbitals of Ho/ Yb atoms near E_F are found to be considerably higher in the valance bands than other orbitals. These observations suggest that 4f orbitals of Ho/ Yb atoms play pivotal roles in enhancing the photocatalytic activities of the compounds in line with our experimental observations (*vide supra*).

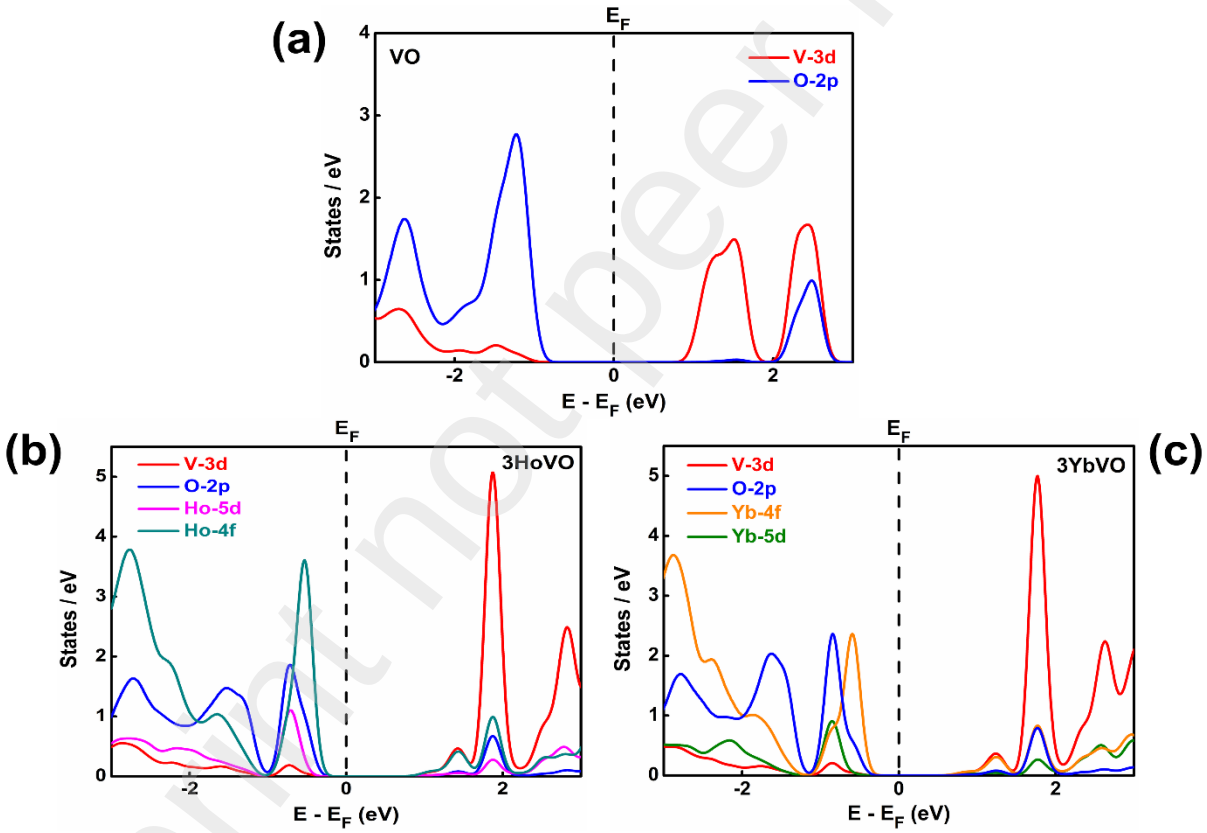

Figure 19. *Orbital resolved PDOS of* ***(a)*** *pristine and 3%* ***(b)*** *Ho,* ***(c)*** *Yb doped - V_2O_5 compounds as obtained from PBEsol+U level of theory. [The Fermi energy E_F is marked with vertical dashed lines]*

4. Conclusions

The Ho and Yb doped V_2O_5 have been produced using an environment-friendly facile mild hydrothermal method, and the effect of doping elements on the photocatalytic activity of V_2O_5 has been studied in comparison with pristine V_2O_5. The doping of RE ions raises the absorption in the UV range due to their unfilled orbitals and customizes oxygen vacancies by creating a charge imbalance in the crystal to reimburse the charge imbalance, enhancing the absorption. The highest relative absorption (RA) and absorption edge (AD) are estimated at 3 mol.% Yb doped V_2O_5 sample, Consequently, the highest degradation efficiency and rate constants are also determined for 3YbVO of 95% and 22, respectively. The bandgap of doped samples, as attained from experimental/ DFT studies, decreases with increasing percentages of dopant, and the highest changes are determined at 2.16/ 2.15 eV (3HoVO) and 2.17/ 2.10 eV (3YbVO), which is approved by the higher RA and AD values estimated for 3YbVO. It is noteworthy that the significant effect of pH on degradation has been studied in detail. The improvement of degradation efficiency estimates exponentially from 11% to 52% by varying the pH level from 5.5 to 7.0. The findings revealed that the maximum efficiency can be achieved for a pH of 7.0, which indicates that the neutral condition or slightly alkaline medium is good for getting better photodegradation efficiency of V_2O_5. The photocatalytic study in detail with doped RE ions has been uncovered, and the highest degradation efficiency is found to be 93% and 95% for the 3 mol.% of Ho and 3 mol.% of Yb-doped V_2O_5 samples, respectively, within 2 hours. The study suggests that 3YbVO and 3HoVO can be considered very efficient catalysts for mitigating serious environmental pollutant issues.

Conflicts of interest

The authors are declared no conflicts of interest.

Data availability

The datasets generated during the current study are available from the corresponding authors on a reasonable request.

Author contributions statement:

M. H. Kabir: Conceptualization, Methodology, Investigation, Software, Data Analysis, Writing-Original draft preparation, Reviewing and Editing. **M. Z. Hossain**: Photocatalytic experiment, **M. A. Jalil**: Photocatalytic experiment and Reviewing, **S. Ghosh**: First-principle DFT calculations, Writing Computational Methodology, Reviewing and Editing, **M.M. Hossain**: Reviewing and Editing, **M. A. Ali:** Reviewing and Editing, **M. U. Khandaker:** Reviewing and Editing, **D. Jana**: Reviewing and Editing, **M. M. Rahman and M. K. Hossain**: Reviewing and Editing, **J. Chowdhury**: Writing Computational Methodology, Data Analysis, Reviewing and Editing, **M.M. Uddin**: Supervision, Conceptualization, Original draft preparation, Reviewing and Editing.

Acknowledgement

The authors are grateful to the Directorate of Research and Extension (DRE), Chittagong University of Engineering and Technology (CUET), Chattogram-4349, Bangladesh and University of Grants Commission (UGC) for arranging financial assistance under grant numbers CUET DRE (CUET/DRE/2018-19/PHY/008) and 37.01.0000.073.07.017.22.209 for arranging the financial support for this work. We are also thankful for the laboratory support of the Materials Science Division, Atomic Energy Centre, Dhaka 1000, Bangladesh for the experimental support. Joydeep Chowdhury and Swarup Ghosh sincerely acknowledge the DST-FIST programme, Department of Physics, Jadavpur University and Bioinformatics Resources and Applications Facility (BRAF), C-DAC, Pune for using the computational facilities. Swarup Ghosh also expresses his thanks to the University Grants Commission, Government of India for providing the UGC-NET award in form of the senior research fellowship.

References

[1] K. Sarayu, S. Sandhya, Current technologies for biological treatment of textile wastewater-A review, Appl Biochem Biotechnol. 167 (2012). https://doi.org/10.1007/s12010-012-9716-6.

[2] J.J. Rueda-Marquez, I. Levchuk, P. Fernández Ibañez, M. Sillanpää, A critical review on application of photocatalysis for toxicity reduction of real wastewaters, J Clean Prod. 258 (2020). https://doi.org/10.1016/j.jclepro.2020.120694.

[3] L. Lin, W. Jiang, L. Chen, P. Xu, H. Wang, Treatment of produced water with photocatalysis: Recent advances, affecting factors and future research prospects, Catalysts. 10 (2020). https://doi.org/10.3390/catal10080924.

[4] H. Chen, L. Wang, Nanostructure sensitization of transition metal oxides for visible-light photocatalysis, Beilstein Journal of Nanotechnology. 5 (2014). https://doi.org/10.3762/bjnano.5.82.

[5] R. Gusain, K. Gupta, P. Joshi, O.P. Khatri, Adsorptive removal and photocatalytic degradation of organic pollutants using metal oxides and their composites: A comprehensive review, Adv Colloid Interface Sci. 272 (2019). https://doi.org/10.1016/j.cis.2019.102009.

[6] A. Zaleska-Medynska, Metal oxide-based photocatalysis: Fundamentals and prospects for application, 2018. https://doi.org/10.1016/C2016-0-01872-7.

[7] T.K. Le, P. v. Pham, C.L. Dong, N. Bahlawane, D. Vernardou, I. Mjejri, A. Rougier, S.W. Kim, Recent advances in vanadium pentoxide (V2O5) towards related applications in chromogenics and beyond: fundamentals, progress, and perspectives, J Mater Chem C Mater. 10 (2022). https://doi.org/10.1039/d1tc04872d.

[8] R. Alrammouz, M. Lazerges, J. Pironon, I. bin Taher, A. Randi, Y. Halfaya, S. Gautier, V2O5 gas sensors: A review, Sens Actuators A Phys. 332 (2021). https://doi.org/10.1016/j.sna.2021.113179.

[9] A. Kim, G. Kalita, J.H. Kim, R. Patel, Recent development in vanadium pentoxide and carbon hybrid active materials for energy storage devices, Nanomaterials. 11 (2021). https://doi.org/10.3390/nano11123213.

[10] J. Yao, Y. Li, R.C. Massé, E. Uchaker, G. Cao, Revitalized interest in vanadium pentoxide as cathode material for lithium-ion batteries and beyond, Energy Storage Mater. 11 (2018). https://doi.org/10.1016/j.ensm.2017.10.014.

[11] M. Rafique, M. Hamza, M.B. Tahir, S. Muhammad, A.G. Al-Sehemi, Facile hydrothermal synthesis of highly efficient and visible light-driven Ni-doped V2O5 photocatalyst for degradation of Rhodamine B dye, Journal of Materials Science: Materials in Electronics. 31 (2020). https://doi.org/10.1007/s10854-020-03844-3.

[12] K. Karthik, M.P. Nikolova, A. Phuruangrat, S. Pushpa, V. Revathi, M. Subbulakshmi, Ultrasound-assisted synthesis of V2O5 nanoparticles for photocatalytic and antibacterial studies, Materials Research Innovations. 24 (2020). https://doi.org/10.1080/14328917.2019.1634404.

[13] Z.Y. Li, Q.H. Wu, The effects of oxygen vacancies on the electronic properties of V 2O 5-x, Journal of Materials Science: Materials in Electronics. 19 (2008). https://doi.org/10.1007/s10854-007-9506-z.

[14] J. Zhang, H. Zhang, M. Liu, Q. Xu, H. Jiang, C. Li, Cobalt-stabilized oxygen vacancy of V2O5 nanosheet arrays with delocalized valence electron for alkaline water splitting, Chem Eng Sci. 227 (2020). https://doi.org/10.1016/j.ces.2020.115915.

[15] S. Zhu, D. Wang, Photocatalysis: Basic principles, diverse forms of implementations and emerging scientific opportunities, Adv Energy Mater. 7 (2017). https://doi.org/10.1002/aenm.201700841.

[16] A. Mehtab, J. Ahmed, S.M. Alshehri, Y. Mao, T. Ahmad, Rare earth doped metal oxide nanoparticles for photocatalysis: A perspective, Nanotechnology. 33 (2022). https://doi.org/10.1088/1361-6528/ac43e7.

[17] N. Bashir, S. Zulfiqar, S. Munir, M.M. Ibrahim, M.F. Abou Taleb, S.M. El-Bahy, M. Suleman, M. Shahid, Sodium doped-V2O5 nanorods for visible light irradiated photocatalytic performance for the degradation of Rh-dye, Ceram Int. 48 (2022). https://doi.org/10.1016/j.ceramint.2021.12.312.

[18] M. Panagopoulou, D. Vernardou, E. Koudoumas, N. Katsarakis, D. Tsoukalas, Y.S. Raptis, Tunable properties of Mg-doped V2O5 thin films for energy applications: Li-ion batteries and electrochromics, Journal of Physical Chemistry C. 121 (2017). https://doi.org/10.1021/acs.jpcc.6b09018.

[19] C.C. Wang, C.L. Lu, F.S. Shieu, H.C. Shih, Structure and photoluminescence properties of thermally synthesized V2O5 and al-doped V2O5 nanostructures, Materials. 14 (2021). https://doi.org/10.3390/ma14020359.

[20] Y.X. Wei, Y.B. Ma, M. Chen, W.M. Liu, L. Li, Y. Yan, Electrochemical investigation of electrochromic device based on WO3 and Ti doped V2O5 films by using electrolyte containing ferrocene, Journal of Electroanalytical Chemistry. 807 (2017). https://doi.org/10.1016/j.jelechem.2017.11.007.

[21] C. Peng, F. Xiao, J. Yang, Z. Li, G. Lei, Q. Xiao, Y. Ding, Z. Hu, Carbon-encapsulated Mn-doped V2O5 nanorods with long span life for high-power rechargeable lithium batteries, Electrochim Acta. 192 (2016). https://doi.org/10.1016/j.electacta.2016.01.195.

[22] I. Pradeep, E. Ranjith Kumar, N. Suriyanaranan, C. Srinivas, N. Venkata Rao, Structural, optical and electrical properties of pure and Fe doped V2O5 nanoparticles for junction diode fabrications, Journal of Materials Science: Materials in Electronics. 29 (2018). https://doi.org/10.1007/s10854-018-9024-1.

[23] P.S. Menon, S.A. Thomas, M.P. Anjana, C. Beryl, D. Sajan, G. Vinitha, R. Philip, The role of defects in the nonlinear optical absorption behavior of pristine and Co-doped V2O5 layered 2D nanostructures, J Alloys Compd. 907 (2022). https://doi.org/10.1016/j.jallcom.2022.164413.

[24] M. Rafique, M. Hamza, M.B. Tahir, S. Muhammad, A.G. Al-Sehemi, Facile hydrothermal synthesis of highly efficient and visible light-driven Ni-doped V2O5 photocatalyst for degradation of Rhodamine B dye, Journal of Materials Science: Materials in Electronics. 31 (2020) 12913–12925. https://doi.org/10.1007/s10854-020-03844-3.

[25] Y. Liu, W. Guo, H. Guo, X. Ren, Q. Xu, Cu (II)-doped V2O5 mediated persulfate activation for heterogeneous catalytic degradation of benzotriazole in aqueous solution, Sep Purif Technol. 230 (2020). https://doi.org/10.1016/j.seppur.2019.115848.

[26] N.S. Kumar, J.H. Chang, M.S. Ho, B. Balraj, S. Chandrasekar, B. Mohanbabu, M. Gowtham, D. Guo, K. Mohanraj, Impact of Zn2+ Doping on the Structural, Morphological and Photodiode Properties of V2O5 Nanorods, J Inorg Organomet Polym Mater. 31 (2021). https://doi.org/10.1007/s10904-020-01751-y.

[27] A. Saliman, Synthesis and Characterization of Zr-Doped Vanadium Oxide Nanotubes, American Journal of Chemical Engineering. 6 (2018). https://doi.org/10.11648/j.ajche.20180604.12.

[28] S. Rajeshwari, J.S. Kumar, R.T. Rajendrakumar, N. Ponpandian, P. Thangadurai, Influence of Sn ion doping on the photocatalytic performance of V2O5 nanorods prepared by hydrothermal method, Mater Res Express. 5 (2018). https://doi.org/10.1088/2053-1591/aaab0a.

[29] C. Yan, L. Liu, Sn-doped V2O5 nanoparticles as catalyst for fast removal of ammonia in air via PEC and PEC-MFC, Chemical Engineering Journal. 392 (2020). https://doi.org/10.1016/j.cej.2019.123738.

[30] J.H. Yao, Z.L. Yin, Z.G. Zou, Y.W. Li, Y-doped V2O5 with enhanced lithium storage performance, RSC Adv. 7 (2017). https://doi.org/10.1039/c7ra03885b.

[31] M.A. Centeno, P. Malet, I. Carrizosa, J.A. Odriozola, Lanthanide Doped V2O5/Al2O3 Catalysts: Structure - Activity Relationship in the SCR of NOx, Journal of Physical Chemistry B. 104 (2000). https://doi.org/10.1021/jp993084a.

[32] B. Etemadi, J. Mazloom, F.E. Ghodsi, Phase transition and surface morphology effects on optical, electrical and lithiation/delithiation behavior of nanostructured Ce-doped V2O5 thin films, Mater Sci Semicond Process. 61 (2017). https://doi.org/10.1016/j.mssp.2016.12.035.

[33] G.R. Navyashree, K. Hareesh, D. v. Sunitha, H. Nagabhushana, G. Nagaraju, Photocatalytic degradation performance of Nd3+ doped V2O5 nanostructures, Mater Res Express. 5 (2018). https://doi.org/10.1088/2053-1591/aad373.

[34] C.C. Wang, C.L. Lu, F.S. Shieu, H.C. Shih, Enhanced photoluminescence properties of Ga-doped V2O5 nanorods via defect structures, Chem Phys Lett. 738 (2020). https://doi.org/10.1016/j.cplett.2019.136864.

[35] H. Chaudhary, K. Chaudhary, S. Zulfiqar, M.S. Saif, I.A. Alsafari, I. Shakir, P.O. Agboola, M. Safdar, M.F. Warsi, Fabrication of reduced Graphene Oxide supported Gd3+ doped V2O5 nanorod arrays for superior photocatalytic and antibacterial activities, Ceram Int. 47 (2021). https://doi.org/10.1016/j.ceramint.2021.08.146.

[36] R. Ray Banik, S. Ghosh, J. Chowdhury, Ultralow lattice thermal conductivity, negative thermal expansion, elastic and thermoelectric properties of Lanthanum Nitride: Insights from first-principle calculations, Phys. Scr. 98 (2023) 045920. https://doi.org/10.1088/1402-4896/acc2ef.

[37] S. Le, C. Zhu, Y. Cao, P. Wang, Q. Liu, H. Zhou, C. Chen, S. Wang, X. Duan, V2O5 nanodot-decorated laminar C3N4 for sustainable photodegradation of amoxicillin under solar light, Appl Catal B. 303 (2022). https://doi.org/10.1016/j.apcatb.2021.120903.

[38] N. Wang, Y. Zhang, T. Hu, Y. Zhao, C. Meng, Facile hydrothermal synthesis of ultrahigh-aspect-ratio V2O5 nanowires for high-performance supercapacitors, Current Applied Physics. 15 (2015). https://doi.org/10.1016/j.cap.2015.01.026.

[39] K. Karthik, K. Pradeeswari, R. Mohan Kumar, R. Murugesan, Microwave-assisted V2O5 nanoflowers for efficient lithium-ion battery, Materials Research Innovations. (2020). https://doi.org/10.1080/14328917.2019.1618044.

[40] S. Beke, A review of the growth of V2O5 films from 1885 to 2010, Thin Solid Films. 519 (2011). https://doi.org/10.1016/j.tsf.2010.11.001.

[41] X. Liu, J. Zeng, H. Yang, K. Zhou, D. Pan, V2O5-Based nanomaterials: Synthesis and their applications, RSC Adv. 8 (2018) 4014–4031. https://doi.org/10.1039/c7ra12523b.

[42] T.K. Le, M. Kang, S.W. Kim, A review on the optical characterization of V2O5 micro-nanostructures, Ceram Int. 45 (2019). https://doi.org/10.1016/j.ceramint.2019.05.339.

[43] P. Giannozzi, O. Andreussi, T. Brumme, O. Bunau, M. Buongiorno Nardelli, M. Calandra, R. Car, C. Cavazzoni, D. Ceresoli, M. Cococcioni, N. Colonna, I. Carnimeo, A. Dal Corso, S. de Gironcoli, P. Delugas, R.A. DiStasio, A. Ferretti, A. Floris, G. Fratesi, G. Fugallo, R. Gebauer, U. Gerstmann, F. Giustino, T. Gorni, J. Jia, M. Kawamura, H.-Y. Ko, A. Kokalj, E. Küçükbenli, M. Lazzeri, M. Marsili, N. Marzari, F. Mauri, N.L. Nguyen, H.-V. Nguyen, A. Otero-de-la-Roza, L. Paulatto, S. Poncé, D. Rocca, R. Sabatini, B. Santra, M. Schlipf, A.P. Seitsonen, A. Smogunov, I. Timrov, T. Thonhauser, P. Umari, N. Vast, X. Wu, S. Baroni, Advanced capabilities for materials modelling with Quantum ESPRESSO, J. Phys.: Condens. Matter. 29 (2017) 465901. https://doi.org/10.1088/1361-648X/aa8f79.

[44] P. Giannozzi, O. Baseggio, P. Bonfà, D. Brunato, R. Car, I. Carnimeo, C. Cavazzoni, S. de Gironcoli, P. Delugas, F. Ferrari Ruffino, A. Ferretti, N. Marzari, I. Timrov, A. Urru, S. Baroni, Quantum ESPRESSO toward the exascale, J. Chem. Phys. 152 (2020) 154105. https://doi.org/10.1063/5.0005082.

[45] M.A. Jalil, M.N.I. Khan, S.K. Mandal, F.-U.-Z. Chowdhury, M.M. Hossain, D. Jana, M.S. Alam, M.M. Uddin, Impact of reaction temperatures on the particle size of V2O5 synthesized by facile hydrothermal technique and photocatalytic efficacy in dye degradation, AIP Adv. 13 (2023) 015010. https://doi.org/10.1063/5.0125200.

[46] C.G. BROYDEN, The Convergence of a Class of Double-rank Minimization Algorithms 1. General Considerations, IMA J. Appl. Math. 6 (1970) 76–90. https://doi.org/10.1093/imamat/6.1.76.

[47] R. Fletcher, A new approach to variable metric algorithms, Comput. J. 13 (1970) 317–322. https://doi.org/10.1093/comjnl/13.3.317.

[48] D. Goldfarb, A Family of Variable-Metric Methods Derived by Variational Means, Math. Comp. 24 (1970) 23–26. https://doi.org/10.2307/2004873.

[49] D.F. Shanno, Conditioning of Quasi-Newton Methods for Function Minimization, Math. Comp. 24 (1970) 647–656. https://doi.org/10.2307/2004840.

[50] A. Dal Corso, Pseudopotentials periodic table: From H to Pu, Comput. Mater. Sci. 95 (2014) 337–350. https://doi.org/https://doi.org/10.1016/j.commatsci.2014.07.043.

[51] J.P. Perdew, A. Ruzsinszky, G.I. Csonka, O.A. Vydrov, G.E. Scuseria, L.A. Constantin, X. Zhou, K. Burke, Restoring the Density-Gradient Expansion for Exchange in Solids and Surfaces, Phys. Rev. Lett. 100 (2008) 136406. https://doi.org/10.1103/PhysRevLett.100.136406.

[52] D.O. Scanlon, A. Walsh, B.J. Morgan, G.W. Watson, An ab initio Study of Reduction of V2O5 through the Formation of Oxygen Vacancies and Li Intercalation, J. Phys. Chem. C. 112 (2008) 9903–9911. https://doi.org/10.1021/jp711334f.

[53] M. Neelima, S. Vandana, A. Kathirvel, M. Sivakumar, A.U. Maheswari, Titanium doped V2O5 nanostructures by chemical synthesis for photocatalytic performance enhancement, Optik (Stuttg). 252 (2022). https://doi.org/10.1016/j.ijleo.2021.168516.

[54] R. Suresh, K. Giribabu, R. Manigandan, S. Munusamy, S. Praveen Kumar, S. Muthamizh, A. Stephen, V. Narayanan, Doping of Co into V2O5 nanoparticles enhances photodegradation of methylene blue, J Alloys Compd. 598 (2014) 151–160. https://doi.org/10.1016/j.jallcom.2014.02.041.

[55] M.H. Kabir, H. Ibrahim, S.A. Ayon, M.M. Billah, S. Neaz, Structural, nonlinear optical and antimicrobial properties of sol-gel derived, Fe-doped CuO thin films, Heliyon. 8 (2022). https://doi.org/10.1016/j.heliyon.2022.e10609.

[56] K.V. Kumar, K. Porkodi, F. Rocha, Langmuir-Hinshelwood kinetics - A theoretical study, Catal Commun. 9 (2008). https://doi.org/10.1016/j.catcom.2007.05.019.

[57] I.K. Konstantinou, T.A. Albanis, Photocatalytic transformation of pesticides in aqueous titanium dioxide suspensions using artificial and solar light: Intermediates and degradation pathways, Appl Catal B. 42 (2003). https://doi.org/10.1016/S0926-3373(02)00266-7.

[58] A. Houas, H. Lachheb, M. Ksibi, E. Elaloui, C. Guillard, J.M. Herrmann, Photocatalytic degradation pathway of methylene blue in water, Appl Catal B. 31 (2001). https://doi.org/10.1016/S0926-3373(00)00276-9.

[59] S. Rani, M. Aggarwal, M. Kumar, S. Sharma, D. Kumar, Removal of methylene blue and rhodamine B from water by zirconium oxide/graphene, Water Science. 30 (2016). https://doi.org/10.1016/j.wsj.2016.04.001.

[60] S.K. Jayaraj, V. Sadishkumar, T. Arun, P. Thangadurai, Enhanced photocatalytic activity of V2O5 nanorods for the photodegradation of organic dyes: A detailed understanding of

the mechanism and their antibacterial activity, Mater Sci Semicond Process. 85 (2018). https://doi.org/10.1016/j.mssp.2018.06.006.

[61] X. Yong, M.A.A. Schoonen, The absolute energy positions of conduction and valence bands of selected semiconducting minerals, American Mineralogist. 85 (2000). https://doi.org/10.2138/am-2000-0416.

[62] D. Rathore, S. Ghosh, J. Chowdhury, S. Pande, Fe-Doped NiCo2Se4 Nanorod Arrays as Electrocatalysts for Overall Electrochemical Water Splitting, ACS Appl. Nano Mater. 6 (2023) 3095–3110. https://doi.org/10.1021/acsanm.3c00265.

[63] D. Rathore, S. Ghosh, J. Chowdhury, S. Pande, Co-Doped Ni9S8 Nanostructures for Electrocatalytic Water Splitting over a Wide pH Range, ACS Appl. Nano Mater. 5 (2022) 11823–11838. https://doi.org/10.1021/acsanm.2c02842.

[64] J.-W. Rhim, B.-J. Yang, Singular flat bands, Adv. Phys.: X. 6 (2021) 1901606. https://doi.org/10.1080/23746149.2021.1901606.

[65] M. Radecka, M. Rekas, A. Trenczek-Zajac, K. Zakrzewska, Importance of the band gap energy and flat band potential for application of modified TiO2 photoanodes in water photolysis, J. Power Sources. 181 (2008) 46–55. https://doi.org/https://doi.org/10.1016/j.jpowsour.2007.10.082.

[66] J. Wang, S.Y. Quek, Isolated flat bands and physics of mixed dimensions in a 2D covalent organic framework, Nanoscale. 12 (2020) 20279–20286. https://doi.org/10.1039/D0NR04428H.